



The structural, mechanical, and biological variation of silica bioglasses obtained by different sintering temperatures

M. Sarmast Sh¹ · A. B. Dayang Radiah^{1,2} · D. A. Hoey^{3,4,5} · N. Abdullah¹ · H. S. Zainuddin¹ · S. Kamarudin¹

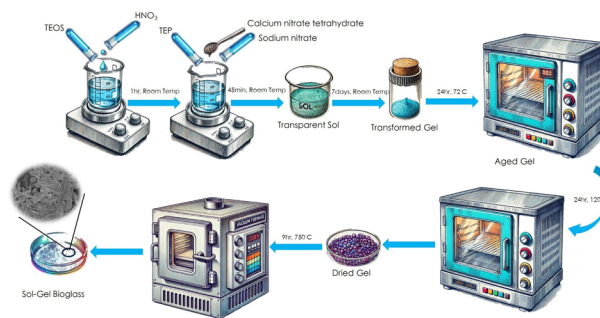
Received: 5 July 2023 / Accepted: 2 July 2024

© The Author(s), under exclusive licence to Springer Science+Business Media, LLC, part of Springer Nature 2024

Abstract

The challenges of forming a crystalline phase within 45S5 Bioglass[®] (45% SiO₂-24.5% CaO-24.5% Na₂O-6% P₂O₅ mol%) and its subsequent influence on the bioactivity of the bioglass were studied in this research. Bioglasses were sintered at 1400, 750, and 550 °C, using both melting and sol-gel methods. The different responses of bioglasses to different sintering temperatures were revealed. Particularly, increased crystallinity was observed in sol-gel-derived bioglass sintered at 750 °C, indicating a denser and more ordered structure. This crystalline architecture facilitated enhanced bioactivity, as demonstrated by increased hydroxyapatite deposition when immersed in simulated body fluid (SBF). Furthermore, superior mechanical properties and biocompatibility were achieved with this temperature regime, making it a prime candidate for bone regeneration applications. The bioglass sintered at 750 °C exhibited an accelerated degradation rate associated with its porosity, potentially contributing to faster material resorption in vivo. Its antibacterial efficacy against *E. coli* and *S. aureus* was also noted, and in vitro studies with MTT assay confirmed that the optimized sol-gel bioglass meets biocompatibility standards. These findings highlight the potential of fine-tuning the sintering temperature to modulate the crystallinity of bioglasses, thereby enhancing their application scope in bone tissue engineering.

Graphical Abstract



Keywords Bioactive glass · Sol-gel · Sintering Temperature · Crystallinity

✉ A. B. Dayang Radiah
dradiah@upm.edu.my

¹ Department of Chemical and Environmental Engineering, Faculty of Engineering, Universiti Putra Malaysia, Serdang, Selangor, Malaysia

² Institute of Nanomaterial and Nanotechnology, Universiti Putra Malaysia, Serdang, Selangor, Malaysia

³ Trinity Centre for Biomedical Engineering, Trinity Biomedical Sciences Institute, Trinity College Dublin, Dublin, Ireland

⁴ Department of Mechanical, Manufacturing, and Biomedical Engineering, School of Engineering, Trinity College, Dublin, Ireland

⁵ Advanced Materials and Bioengineering Research Centre, Trinity College Dublin & RCSI, Dublin, Ireland

Highlight

- Bioglasses were sintered at three different temperatures: 550, 750, and 1400 °C.
- The sol-gel-derived sintered at 750 °C exhibited increased crystallinity.
- This increased crystallinity resulted in enhanced mechanical properties, biocompatibility, antibacterial efficacy, and accelerated degradation.

1 Introduction

Silica-based bioglasses have gained significant attention in the field of biomaterials due to their unique properties and potential applications in bone grafting and tissue engineering. The development and characterization of bioglasses synthesized using different techniques have been subjects of extensive research [1–3]. Among these techniques, the melting and sol-gel methods have emerged as prominent approaches for producing bioglasses with tailored properties.

The melting method involves high-temperature melting and quenching, while the sol-gel technique utilizes the controlled hydrolysis and condensation of precursor materials to form a gel [4]. The choice of the synthesis method and sintering temperature plays a crucial role in determining the structure, morphology, crystallinity, and bioactivity of the resulting bioglasses [5, 6]. Understanding the effects of sintering temperature on bioglass properties is essential for optimizing their performance in biomedical applications.

Previous studies have investigated the influence of sintering temperature on the properties of bioglasses. For instance, Bellucci et al. [7] reported that the sintering temperature affected the crystallization behavior and post-sintering bioactivity of sol-gel derived bioglasses. Lefebvre et al. [8] demonstrated that variations in sintering temperature led to structural transformations in 45S5 bioactive glass. Furthermore, Chitra et al. [9] highlighted the correlation between sintering temperature, crystallization, and cytocompatibility of bioglasses.

In this study, we aim to provide a comprehensive investigation of the melting and sol-gel techniques, with a particular emphasis on analyzing the impact of sintering temperature on the properties of silica bioglasses. The findings of this study will contribute to a better understanding of the relationship between synthesis parameters and the resulting properties of bioglasses.

This research investigated how sintering temperatures affect silica bioglasses fabricated via melting and sol-gel techniques. Changing the sintering temperature allows for specific control over the crystallinity of bioglasses, directly impacting their structural, mechanical, and biological properties. This comprehensive understanding provides tailoring bioglass properties for bone tissue engineering, presenting a strategic method to enhance material functionality through sintering temperature modulation.

2 Materials and methods

In this study, the synthesis of the bioglass was carried out based on the reported compositions 45% SiO₂-24.5% CaO-24.5% Na₂O-6% P₂O₅ mol% same as a trademarked 45S5 Bioglass[®] designed by Larry Hench [10–12]. The synthesis process involved several steps. Initially, tetraethyl orthosilicate (TEOS, 98%, Sigma Aldrich, China) was mixed with 1M HNO₃ (65%, R&M Chemicals, Malaysia) at a room temperature for 1 h. Triethyl phosphate (TEP, 99%, R&M Chemicals, Malaysia) was then added dropwise to the solution. Calcium nitrate tetrahydrate (Ca(NO₃)₂·4 H₂O, R&M Chemicals, Malaysia) and sodium nitrate (NaNO₃, 99%, R&M Chemicals, Malaysia) were gradually added to the mixture until a transparent solution (sol) was formed. The sol was then stored in a sealed container at room temperature for seven days to allow gel formation. The gel was aged in a vacuum oven (ED56, Binder) for 24 h at 70 ± 2 °C, followed by drying in an oven at 120 °C for another 24 h to remove free water. The dried gel was subsequently sintered at two different temperature (550 and 750 °C) for 9 h in a vacuum furnace (CWF 12/13, Carbolite, UK) to obtain the bioglass powder. The commercial 45S5 Bioglass[®], which was prepared by the melting method at 1400 °C, was purchased from Apatech Nano Technology, Yazd, Iran. The bioglass samples produced in this study were referred to as BG45S5, BG550, and BG750.

Two types of tablets were used in this study: Disk-shaped tablet with a diameter of 10 ± 2 and a height of 2 ± 1 mm was fabricated in accordance with the ISO 23317-2007 for bioactivity, biodegradation, and water intake assessments. According to the ASTM standard D638 (Type V), the tablet with a diameter of 5 ± 0.5 mm and length of 10 ± 0.5 mm was fabricated for the mechanical testing. The molds (with the given dimensions and made of stainless steel) were filled with 1 ± 0.5 g of bioglass powder. The mixture was compressed using the press machine (Instron 3365, Instron, America) with load pressure of 5 MPa and dwell time of 60 s [5, 13, 14].

The thermal properties of the bioglass samples, including the bioglass transition temperature (T_g) and crystallization temperature (T_c), were determined using thermogravimetric analysis (TGA) and differential scanning calorimetric (DSC) unit (TGA-DSC HT 3, Mettler Toledo, Malaysia). For the analysis, 7 mg of each sample was placed in the alumina crucible and measured under nitrogen flow at a heating rate of 10 °C/min from 50 to 1400 °C.

FTIR spectroscopy (Spectrum 100, Perkin Elmer) was employed to analyze the inter-molecular interactions among the components of the bioglasses. Spectra were recorded in the range of 500 to 4000 cm^{-1} . The bioglass sample was mixed with 300 mg of KBr (infrared grade) and formed into a pellet before analysis.

The morphology of the synthesized samples before and after immersing in SBF solution was examined using a Field Emission Scanning Electron Microscope (FESEM) (Nova Nanosem 230, FEI, USA) operated at a voltage of 20 kV. Prior to characterization, all samples were gold coated. FESEM images magnified at 2500x and insets at 25000x. Simultaneous energy-dispersive X-ray spectroscopy (EDX) analysis (Oxford Instruments, Max20, UK) was conducted at specific points on the samples to identify the presence of specific elements, namely Si, Ca, P, Na, and O.

The X-ray diffraction (XRD) (X'Pert Pro PANalytical, PW 3040/60, Netherlands) profiles were acquired to identify the crystalline phases of bioglasses before and after soaking in SBF solution. The instrument operated at room temperature, the current and voltage were 32 A and 40 kV, with Cu K radiation. The XRD scans were conducted within a $2\theta = 20^\circ\text{--}70^\circ$.

Based on the XRD data, the average crystallite size and crystallinity of the formed powder were calculated. The average crystallite size (nm) was calculated using the Scherrer equation (Eq. 1), where K is the Scherrer constant (0.9), λ is the wavelength of the X-ray source (0.15406 nm), β is the estimated value of full width at half maximum, and θ is the peak position in radians.

$$\text{Crystallite Size} = \frac{K\lambda}{\beta \cos\theta} \quad (1)$$

The degree of crystallinity was determined by calculating the ratio of the integrated area of all crystalline peaks to the total integrated area under the XRD peaks using Eq. 2, where I_c represents the integrated intensity corresponding to the combeite crystalline phase of the sample, and I_{c^*} represents the integrated intensity corresponding to the 45S5 Bioglass[®].

$$\% \text{Crystallinity} = \frac{I_c}{I_{c^*}} \times 100 \quad (2)$$

The porosity and apparent density of the produced BG samples were measured using the ethanol displacement test. The specimens for the porosity and density measurement were prepared based on the sample description outlined in ISO 23317-2007 guide. The initial weight (W_i) of the BG sample was recorded for the porosity analysis. The sample was then immersed in a container with a known amount of ethanol (V_1) and left for 15 min to allow the ethanol to fill all pores in the sample. The combined volume of ethanol

and sample was denoted as V_2 . After removing the sample from the ethanol solution, the final mass was weighed and recorded (W_f), and the volume of ethanol remaining in the container was recorded as V_3 . Porosity and density values were calculated using Eqs. 3 and 4, respectively [15]. The internal structures of the produced specimens were not assessed, which is a limitation of the analyses performed in this work.

$$\% \text{Porosity} = \frac{V_1 - V_3}{V_2 - V_3} \times 100 \quad (3)$$

$$\text{Density} = \frac{W_f}{V_2 - V_1} \quad (4)$$

The Brunauer–Emmett–Teller (BET) (Quantachrome, Autosorb-1, USA) was used to ascertain bioglasses' specific surface area, pore volume, and pore size distribution. The pore size distribution was derived from the N_2 desorption segment of the obtained N_2 adsorption-desorption measurements conducted at 77 K under vacuum.

The swelling test was performed by immersing disc-shaped BG samples in distilled water. The samples were shaped into discs and immersed in 25 ml of distilled water in a polyethylene bottle container, which was then placed in an incubator at 37 °C for a week without agitation. The discs were periodically removed from the containers, excess water was gently removed by wiping the surface with tissue papers, and the changes in the shape of the discs (swelling) were measured. The water intake was calculated using Eq. 5, where W_i represents the initial mass of the sample, and W_f represents the final weight of the sample.

$$\Delta W\% = \frac{W_f - W_i}{W_i} \times 100 \quad (5)$$

The solubility of the samples was measured by drying the samples after the swelling test at room temperature for 24 h in a desiccator and reweighing them. The solubility was calculated as the weight loss per unit area using Eq. 6, where M_i is the initial mass of the sample, M_t is the mass of the sample at a specific time point, and A is the surface area (mm^2).

$$\Delta M = \frac{M_t - M_i}{A} \quad (6)$$

The mechanical properties were evaluated using a compression test according to ASTM Standard D638 (Type V). At least five specimens were tested for each BG sample using a dual column tabletop universal testing system (Instron 3365, Instron, America) equipped with a 50N load cell. The tests were conducted at a crosshead speed of 5 mm/min.

In vitro bioactivity was evaluated by examining apatite formation on the material surface after exposure to simulated body fluid (SBF). The SBF solution was prepared

according to the method described by Kokubo and ISO 23317-2014 [16, 17]. The samples were placed in a polyethylene bottle containing 32 mL of SBF solution without agitation and incubated at 37 °C for specified time points (1, 7, 14, 21, and 28 days). The volume of the SBF solution was determined using the formula, where V_s represents the volume of SBF solution in mL and S_a is the surface area of the tablets in mm².

$$V_s = S_a / 10 \quad (7)$$

Two different solution treatments were applied to each sample: (1) the "NR" treatment, where there was no solution refreshment or adjustment, and (2) the "R" treatment, where the solutions were refreshed every 24 h to maintain a pH of 7.42. After the incubation period, the samples were rinsed with distilled water and dried in a desiccator for 24 h at room temperature. The formation of hydroxyapatite on the surface was examined using a FESEM (Nova Nanosem 230, FEI, USA) and analyzed using an X-ray Diffractometer (X'Pert Pro PANalytical, PW 3040/60, Netherlands).

The concentration of released ions from the BG particles in SBF solution, such as Ca, was analyzed using Inductively Coupled Plasma-Optical Emission Spectroscopy (ICP-OES) (PerkinElmer Optima, 7300 DV instrument, USA). Fresh SBF solution was used as a control.

The In vitro degradation study of the BGs was performed in phosphate-buffered saline (PBS) solution at pH 7.4 and 37 °C for a week. The weight of each specimen was measured initially, and then the samples were periodically removed from the solution, washed, and dried. The degradation was calculated using Eq. 8, where M_i and M_f represent the initial and final weights of the dried samples, respectively [18].

$$\text{Degradation}\% = \frac{M_i - M_f}{M_i} \times 100 \quad (8)$$

Using a liquid culture method, the antibacterial effectiveness of bioglasses was assessed against Gram-positive *S. aureus* (ATCC[®] 6538) and Gram-negative *E. coli* (ATCC[®] 8739). *S. aureus* were cultured in liquid nutrient broth (NB) medium (NB, Miller, Becton Dickinson, USA). *E. coli* were cultured in liquid LB broth (LB Broth, Lennox, USA). Bacteria were grown in their medium overnight at 37 °C on an orbital shaker. Prior to the experiment, the bacterial suspension was diluted to approximately 10⁸ CFU/mL. Next, 10 mg of bioglasses were sterilized using a UV lamp for 1 h at room temperature. Subsequently, the bioglasses were incubated at 37 °C and stirred at 150 rpm with 1 ml of the bacterial suspension. After 18 h, the optical densities of the bacterial solution containing one of the bioglasses (OD_s) were measured at 600 nm with a UV spectrophotometer (UV-1800, Shimadzu, Japan) and compared to the Samples of bacteria without bioglass (OD_c)

used as a control. The degree of bacterial inhibition was determined using the following formula [18]:

$$\text{Bacterial inhibition}\% = \frac{OD_c - OD_s}{OD_c} \times 100 \quad (9)$$

The pH of the bacterial suspension containing the bioglass samples was measured to monitor changes during the antibacterial evaluation. Before incubation, the initial pH of the bacterial suspension was recorded using a pH meter (PH-B200E, Infitek, China) at room temperature. After 18 h of incubation with the bioglass samples at 37 °C, the pH of the suspension was measured again. This step ensured that any observed antibacterial effects could be correlated with changes in pH, providing insights into the bioglass's interaction with the bacterial environment.

The viability of MC3T3 cells (mouse embryonic fibroblast cells) was assessed using the MTT assay. The MC3T3 cells was purchase from the Institute of Bioscience, Universiti Putra Malaysia. To perform the assay, 0.1 g of bioglass powders were suspended in 2 mL of medium and incubated at 37 °C overnight to obtain the extract. The MC3T3 cells were treated with this extract, and their viability was evaluated using the MTT assay. The MTT assay is a colorimetric method that involves the conversion of a yellow tetrazolium salt, 3-{4,5 dimethylthiazol-2-yl}-2,5-diphenyl tetrazolium bromide, into purple formazan crystals by the mitochondrial esterase enzyme in metabolically active cells [18–20]. For the assay, 7 × 10³ cells/mL were prepared and plated onto 96-well plates at a volume of 100 μL per well. The cells were treated with different dilutions of the bioglass extract (25, 50, and 100%). Wells with medium alone were used as controls. After incubating the plates for 24 h at 37 °C in a 5% carbon dioxide atmosphere, the extract was removed, and 100 μL of MTT working solution (1 in 10 dilutions, stock concentration of 5 mg/mL, Sigma Aldrich) was added to each well. The plates were then incubated in a 95% humidified atmosphere at 37 °C for 3 h. After incubation, the MTT reagent was removed, and the wells were gently rinsed with PBS. Next, 100 μL of dimethyl sulfoxide (DMSO) was added to each well and incubated for 5 min at 37 °C in a shaker to solubilize the formazan pigment produced. The formazan solution's optical density (OD) was measured at a wavelength of 570 nm using an ELISA reader (TECAN, Switzerland). Higher optical density values indicate a higher concentration of living cells in the solution [18].

$$\text{Cell Viability}\% = \frac{\text{Absorbance sample (mean)}}{\text{Absorbance control (mean)}} \times 100 \quad (10)$$

One-way ANOVA was used to analyze the data with Holm-Bonferroni post-hoc test. Values are means ± s.d. for

three independent replicates. * $P \leq 0.05$, ** $P \leq 0.01$ and *** $P \leq 0.001$.

3 Results and discussion

3.1 Thermogravimetric analysis

The thermal behaviors of the bioglasses after sintering were assessed using TGA/DSC unit to identify suitable heat treatment temperatures (Fig. 1). The TGA/DSC analysis highlighted the influence of the fabrication method and sintering temperature on amorphous and crystallinity behaviors of the produced bioglass. These findings highlight the importance of careful control over processing parameters to tailor the properties of bioglasses for specific biomedical applications.

The DSC function was used to evaluate the glass transition (T_g) and crystallization (T_c) conditions which are critical events that occurred during heating. These points depict the transformation of the glass from a supercooled liquid to an amorphous solid and then to a crystalline structure. T_x indicates the temperature at which crystallization begins, while ΔT measures the temperature range over which crystallization occurs ($\Delta T = T_c - T_x$) [21]. These pivotal transitions, clearly depicted in the DSC plots, are instrumental in understanding the crystalline phase development of each bioglass composition. The TGA functions were used to show mass loss or mass gain during the heating process. These scenarios had been depicted quite well for the bioglass samples tested.

BG45S5, produced via melting, demonstrated exceptional stability with a mere 1.6% of total weight loss when heated up to 1400 °C (Fig. 1a). The DSC spectrum for 45S5 bioglass indicated the removal of alcohol and physically bound water molecules at 42–132 °C, resulting in a minor 0.1% weight loss. Subsequent peaks at 160–188 °C (0.23% weight loss) and 483–1391 °C (broad exothermic peak with 0.4% weight loss) corresponded to the removal of nitrate groups, the degradation of the amorphous structures and the formation of stable and dense crystal, respectively. The increase in weight around 650 °C in the TGA results suggests that the crystallization process had been initiated, potentially preceding to the observed crystallization temperature (T_c) at 1393 °C [9, 18, 22, 23]. The porous melt-derived glasses, like Bioglass 45S5, tends to form crystal at a small sintering window, a limitation that had been highlighted by many researchers [24]. Thus, understanding the thermal behavior of these materials at the respective operating conditions are important. The summarized results of thermal data and compositional analysis obtained from the TGA/DSC unit are as displayed in Table 1.

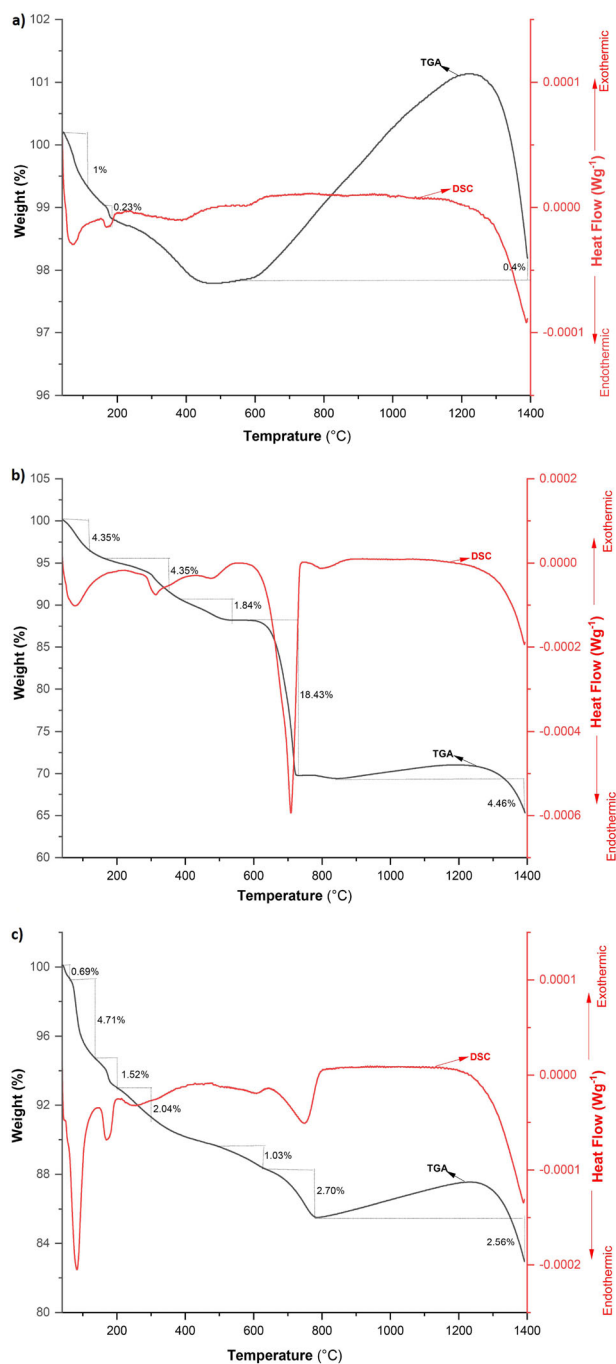


Fig. 1 TGA and DSC curves for (a) Bioglass 45S5 (b) BG-550 and (c) BG-750 (nitrogen atmosphere, 10 °C min⁻¹)

Table 1 TGA/DSC results of bioglasses

Sample	Total Weight Loss (%)	Number of Stages	T_{g1} (°C)	T_{g2} (°C)	T_c (°C)	T_x (°C)	ΔT (°C)
BG45S5	1.6	3	552		1393	983	431
BG550	33.43	5	474				
BG750	15.25	6	237	620	748	428	191

In contrast, BG550 and BG750, sintered using the sol-gel method at 550 and 750 °C, respectively, displayed significantly higher weight losses, indicative of different stages of thermal degradation. BG550, sintered at 550 °C, (Fig. 1b) revealed a weight loss of 4.35% in the first stage (48–162 °C) due to the removal of alcohol, nitrate, and physically bound water molecules. Subsequent stages indicated further nitrate removal, glass transition temperature (T_g) at 474 °C, and bioglass phase changes [18, 25].

BG750 exhibited an even more substantial weight loss of 15.26% across six stages (Fig. 1c). The initial stages involved the evaporation of crystalline water [25]. Mass loss of about 6.22% were reported in the subsequent stages (59–192 °C) due to the removal of water and nitrate groups [9, 18, 25]. The glass transition temperatures (T_{g1} at 237 °C and T_{g2} at 543–644 °C) were observed, along with a crystallization peak (T_c) at 748 °C [18].

The differences in weight loss between samples sintered at different temperatures highlight the complex interaction between processing conditions, composition, and thermal behavior of bioglasses. The TG and DSC analyses of the bioactive glasses, namely the BG550 and BG750 samples, were performed after the sintering process to investigate their thermal stability and crystallinity. The high weight loss of the samples after the sintering condition may result from the loss of residual organic compounds, moisture, and amorphous content. Exposure to high temperature condition during the analysis could also induce additional chemical reactions, such as oxidation or decomposition of residual inorganic species as well as transformation of amorphous to crystal which then affected the structural arrangements within the glass matrix [18, 25].

The sintering temperature of 750 °C produced a stable silica bioglass with, excellent bioactivity and no nitrogen content [11, 18].

3.2 Fourier transform infrared (FTIR) spectroscopy

The effect of different chemical compositions and sintering temperatures on the chemical structure and functional groups in sol-gel and melting method bioglasses was investigated using FTIR analysis. The FTIR spectra of the sol-gel synthesized bioglasses confirm that the obtained bioglasses maintain functional groups that are characteristic of silica bioactive glass such as Si–O–Si bending and stretching vibrations, across all samples [26, 27]. Figure 2 and Table 2 present the FTIR spectra of three bioglass samples: melting and sol-gel.

Moisture-related absorption, indicated by the 1643 cm^{-1} peak, was uniquely observed in BG550, suggesting molecular water entrapped in the glass matrix when sintered at 550 °C [19, 28]. This feature emphasizes the lower densification at this temperature, which may affect the bioactive

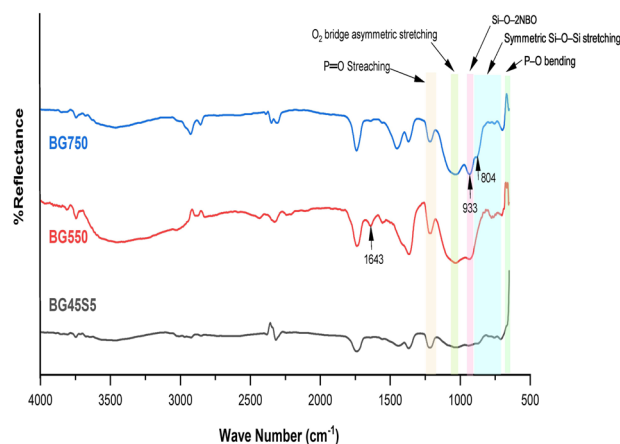


Fig. 2 FTIR spectra of BG45S5, BG550, and BG750

response of bioglass. Across the bioglasses, Si–O–Si bending (1216–1209 cm^{-1}) and asymmetric stretching vibrations (1085–1061 cm^{-1}) were consistently present, indicating the formation of the silicate network [26–30].

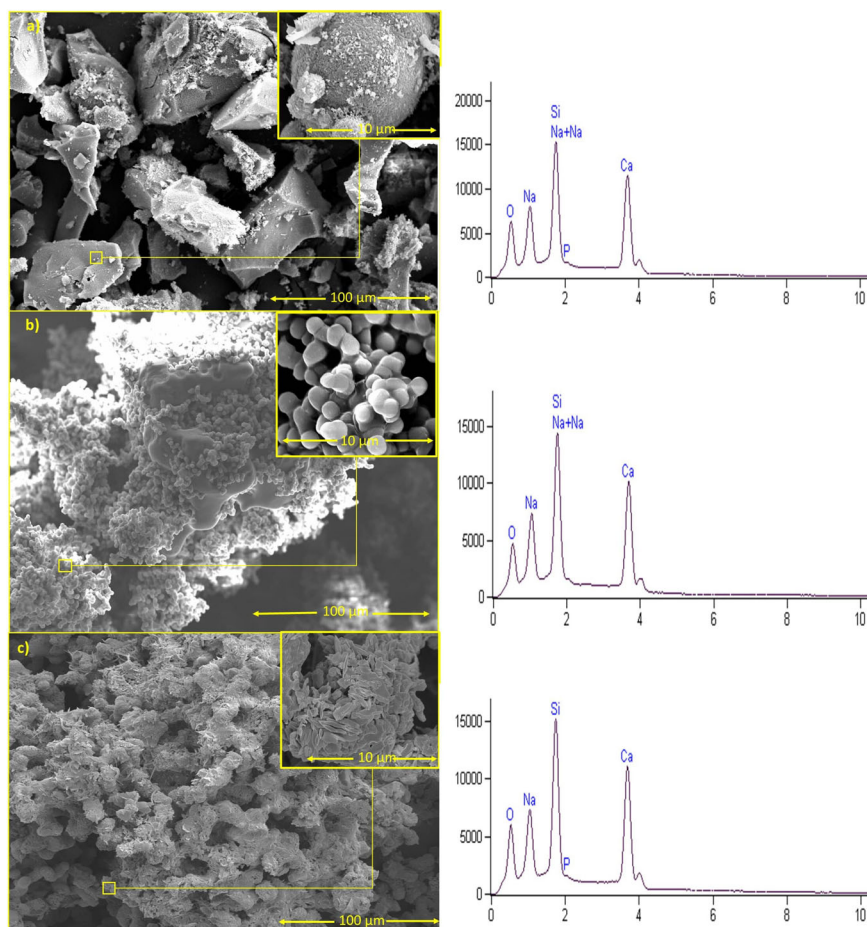
As seen in BG750 and BG45S5 at higher sintering temperatures, the silicate absorption bands broaden, suggesting a more interconnected and possibly more crystalline silicate structure. The stretching vibrations in the 1034–1030 cm^{-1} region indicate Si–O–Si bonds, while the vibrational modes in the 925–950 cm^{-1} range signify the formation of non-bridging oxygen (NBO) through Si–O–2NBO bonds, indicative of network modifiers such as Ca^{+2} and Na^{+1} [18, 28, 30, 31]. A particular feature in BG750 is the presence of a peak at 804 cm^{-1} , which is not observed in the other bioglasses. This peak reflects the symmetric Si–O–Si stretching vibrations involving bridging oxygen atoms, a sign of increased cross-linking in the glass network, which may contribute to a higher degree of crystallinity [26, 32].

Bands in the 775–710 cm^{-1} range depicted Si–O–Si symmetric stretching vibrations of bridging oxygen atoms among tetrahedrons [19, 26, 28, 32, 33]. These bands also reflected the symmetric Si–O–Si stretching vibration in crystalline silicate SiO_4^{-4} , with an additional NBO atom among tetrahedrons evident at 804 cm^{-1} [26]. A peak highlighted the presence of a silica network at 699 cm^{-1} [30]. Furthermore, the P–O bond stretching mode of the phosphate group, observed between 615 and 610 cm^{-1} , indicated a crystalline phosphate phase [18, 29].

BG750 exhibits a higher content of NBO bonds compared to BG45S5 and BG550, as evidenced by the FTIR peaks. The presence of more NBOs is associated with a higher degree of bioactivity and chemical stability, which reduces the likelihood of material degradation or component leaching over time [3, 34]. Consequently, the enhanced oxygen bonding in the BG750 structure may lead to improved chemical stability and, potentially, a more

Table 2 FTIR characteristic bands of the synthesized particles

Wavenumber (cm ⁻¹)	Vibration Mode	References
1643	Presence of Molecular Water; Moisture Absorption Reaction at Glass Surface	[19, 28]
1216–1209	Bending Mode of Si–O–Si	[26, 27]
1085–1061	Asymmetric Stretching of Bridging Oxygen	[28–30]
1034–1030	Si–O–Si Stretching Vibrations	[18, 30, 31]
925–950	Si–O–2NBO (Non-bridging Oxygen) Stretching Vibrations	[18, 28, 31]
804	Attributed to Non-bridging Oxygen	[26]
775–710	Symmetric Si–O–Si Stretching Vibrations Of Bridging Oxygen Atoms Among Tetrahedrons	[26, 28, 32]
699	Presence Of Silica Network	[30]
615–600	P–O Bending Vibrations in PO ₄ ³⁻ Groups	[18, 29]

Fig. 3 FESEM-EDX of (a) BG45S5, (b) BG550 and (c) BG750

favorable bioactive response when compared to its counterparts.

3.3 Morphology analysis

The morphology and elemental composition analysis of the melting method and sol-gel are illustrated in Fig. 3. Bioglass 45S5 (Fig. 3a) shows a rough fracture surface with particle agglomeration and minimal porosity, a morphology

that suggests limited surface crystallization. The reduced particle size and consequent increase in surface charge and reactivity potentially lead to powder agglomeration, a common occurrence in melt-derived glasses [28]. In contrast, BG550 (Fig. 3b) demonstrates soft surfaces, which is not typical for sol-gel-derived bioglasses expected to undergo initial glass transitions and phase separation around 550 °C. The absence of a rough surface may hint at an inhibited crystallization process at this temperature,

Table 3 Porosity, density, and BET analysis results of bioglasses

Samples	%Porosity	Density (g/cm ³)	Surface Area (m ² /g)	Total pore volume (cm ³ /g)	Pore Size (nm)
BG45S5	45.83 ± 1.33	1.00 ± 0.26	2.220	0.035	1.88
BG550	41.67 ± 1.66	0.61 ± 0.33	3.083	0.214	137.63
BG750	52.50 ± 1.45	0.85 ± 0.19	5.459	0.217	79.50

preventing the anticipated phase separation into Si-rich and P-rich phases, thereby resulting in a smoother surface [35, 36]. BG750 presents a porous and well-defined interconnecting structure, indicative of growth crystallization or early polymerization (Fig. 3c). The higher sintering temperature and the acidic conditions of the sol-gel process promote the formation of a more open and interconnected porous network favorable for bioactivity [28].

EDX analysis confirmed the presence of silicon, sodium, and calcium across all samples, vital elements for bioglass functionality in bone scaffolding due to their roles in stimulating cell proliferation and new bone formation [37]. However, the absence of a phosphorus peak in BG550 could be attributed to the suppressed glass phase separation at 550 °C, potentially leading to an underdeveloped P-rich layer [37]. The EDX spectra for BG750 revealed a slight variation in the elemental composition compared to BG45S5, with higher weight percentages of sodium, silicon, and calcium observed. This compositional difference could reflect a more mature crystalline phase formation in BG750, possibly enhancing its bioactive potential.

3.4 Porosity and density analyses

Porosity within bioglass scaffolds is a pivotal factor in tissue regeneration, affecting the delivery of nutrients and oxygen and significantly influencing cell adhesion, proliferation, and differentiation. It also plays a role in the mechanical stability of implants, where larger pores are advantageous for cell growth and nutrient transport. The nature and distribution of porosity, governed by the bioglass pore dimensions, dictate the material's wettability and capability to facilitate the movement of oxygen and essential nutrients to the regenerating tissues [18]. The porosity, density, and pore structure of bioglasses are presented in Table 3.

BG45S5 shows a porosity of approximately 46%, which increases to 52.5% for BG750. Conversely, BG550 demonstrates the lowest porosity at 42%, which correlates with a less porous structure, as observed in the FESEM images. This lack of porosity in BG550 may result from the inhibited phase separation of Si and P at 550 °C, which typically leads to a more heterogeneous structure [8]. Bioactive glass with increased porosity generally exhibits a reduced density, which is evident in the comparative densities of the samples. The melting method's tendency to

cause powder agglomeration results in the highest density for BG45S5 at 1 g/cm³ [28, 38].

BG550 and BG750, with densities of 0.61 and 0.85 g/cm³, respectively, show variations due to their different microstructural characteristics, with BG550's low density also resulting from sample degradation in ethanol. The density of silicate bioglasses is known to be influenced by the concentration of network modifiers within the silicate structure [28, 39].

The BET analysis, particularly for BG750, indicates a nearly 20 times greater surface area than commercial 45S5 Bioglass[®]. This extensive surface area results from the sol-gel process, where the gelation and drying conditions produce a network of continuous pores, varying from interconnected to completely closed, depending on the processing conditions and stabilization temperature. The formation of this three-dimensional polymeric network is facilitated by the condensation reactions of the hydrolyzed tetrafunctional [Si(OH)₄] [4]. In contrast, melt-derived bioglass typically exhibits minimal porosity due to the surface tension during melting and inherent structural heterogeneities. Sol-gel-derived bioglasses, however, can exhibit biomimetic macroporosity conducive to enhanced cell adhesion [40, 41]. Nevertheless, significant reductions in total pore volume during sintering can adversely affect the creation of porous scaffolds suitable for bone regeneration and repair due to the potential for poorly interconnected porosity [7].

The mesoporous nature of the pores in BG750, ranging from 10 nm to 70 nm as per the IUPAC classification of type IV hysteresis, is indicative of the fine control achieved through the sol-gel process and the chosen calcination temperature [42]. These results can be attributed to the sol-gel approach used in sample preparation and the calcination process at 750 °C, which resulted in the formation of homogeneously sized pores upon cooling. 750 °C is an excellent choice for calcination based on the BET data and the FESEM images shown in Fig. 3c. The porous structures of BG750 promote rapid biodegradation, facilitating the formation of new bone [43, 44].

3.5 Crystallinity analysis

Bioactive glasses are typically amorphous; however, they can crystallize upon thermal treatment, altering their bioactivity and mechanical properties, which is crucial for

applications like bone scaffolds [8, 35]. When using sol-gel and melting methods to produce bioglass, three major silicate-based minerals, Wallace, combeite, and cristobalite, are commonly observed as prominent crystalline peaks [45]. Several studies indicate that combeite $\text{Na}_2\text{Ca}_2\text{Si}_3\text{O}_9$ is the primary crystalline phase of 45S5 Bioglass[®] after heat treatment [18, 36, 46]. However, there is uncertainty because 45S5 Bioglass[®] primarily crystallizes in the $\text{Na}_2\text{CaSi}_2\text{O}_6$ phase, instead of $\text{Na}_2\text{Ca}_2\text{Si}_3\text{O}_9$, within the temperature range of 600–700 °C [18, 46]. The high-temperature forms of $\text{Na}_2\text{Ca}_2\text{Si}_3\text{O}_9$ are isostructural, and $\text{Na}_2\text{Ca}_2\text{Si}_3\text{O}_9$ dominates in samples treated at temperatures above 950–1000 °C, with a significant dependence on thermal process parameters [8, 18]. Furthermore, increasing the sintering temperature from 700 to 1000 °C results in combeite-I ($\text{Na}_6\text{Ca}_3\text{Si}_6\text{O}_{18}$) predominance, a crystalline phase dispersed in an amorphous glass matrix. Furthermore, raising the sintering temperature leads to the formation of a crystalline phosphorus-rich apatite-like phase, Silicorhenanite, ($\text{Na}_2\text{Ca}_4(\text{PO}_4)_2\text{SiO}_4$) [46]. Previous research indicates that the presence of phosphorus in a sol solution, followed by the formation of an apatite-like phase, reduces bioactivity. Therefore, the stabilization temperature should be decreased to prevent the formation of this apatite phase and reduce crystallization [8, 11, 36].

The formation of combeite crystals is significant because combeite is a calcium sodium silicate that should not contain phosphorus [10]. Combeite crystal nuclei form when significant heat and mass transfer gradients exist between the phosphorus-rich and silicon-rich phases. In such cases, a phosphorus gradient can form between the crystals and their grain boundaries, or the phosphorus can volatilize [10, 47]. As mentioned earlier, phosphorus-associated clusters in the dispersed phosphorus-rich glassy phase can play various roles in the bulk nucleation of crystals. The P=O bond favors the formation of the phosphate phase in a silicate network, thereby increasing the tendency toward crystallization [47, 48]. P_2O_5 serves a dual role in silicate glasses as a network-forming agent and a substance that promotes bioglass crystallization [8, 10, 47].

Figure 4 shows the XRD patterns for Dried Gel, BG45S5, BG550, and BG750. The XRD pattern of the dried gel, representing bioglass before heat treatment and dried at 120 °C for 24 h, reveals the specific characteristics of a fully amorphous structure. This is obvious in the broad hump without distinct crystalline reflections [46, 49]. Although there might be initial crystallization stages or crystalline phases nucleation, the overall XRD profile indicates an amorphous structure [46]. After the sintering process, the bioglass exhibits a diffraction pattern characteristic of a bioglass structure, indicating a transformation in its crystalline structure, particularly in the $2\theta = 27\text{--}34^\circ$ range. The XRD patterns of all samples after sintering

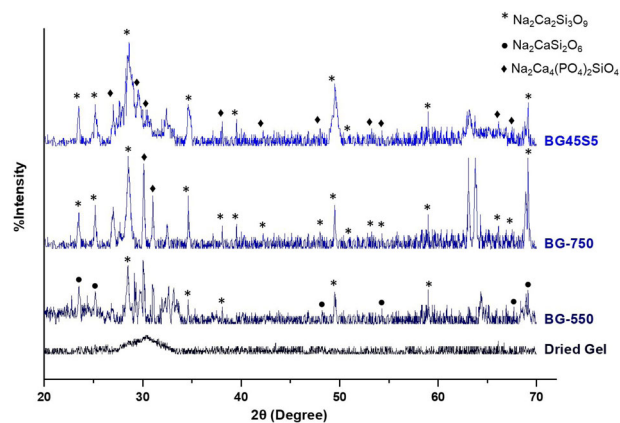


Fig. 4 The X-Ray diffractogram of all bioglass samples

Table 4 The crystallinity and crystalline size of bioglasses

Sample Name	Crystallinity%	Crystalline Size (nm)
BG45S5	32.33 ± 4.3	38.74 ± 2.63
BG550	15.89 ± 3.1	7.67 ± 1.04
BG750	89.27 ± 4.5	28.88 ± 2.41

indicate the presence of the crystalline phases $\text{Na}_2\text{Ca}_2\text{Si}_3\text{O}_9$ (JCPDS code 22-1455), $\text{Na}_2\text{CaSi}_2\text{O}_6$ (PDF code 01-077-2189), and ($\text{Na}_2\text{Ca}_4(\text{PO}_4)_2\text{SiO}_4$) (PDF code 00-032-1053). In the crystalline melting method and sol-gel bioglasses, the patterns match Combeite ($\text{Na}_2\text{Ca}_2\text{Si}_3\text{O}_9$), which possesses a trigonal-trapezohedral class symmetry [8, 10, 36]. Regarding the FTIR results, all samples exhibited the P–O band at 615–600 cm^{-1} . The XRD pattern demonstrates that the fabrication method and sintering temperature directly influence crystallization. Above 550 °C, there is an increased tendency of 45S5 Bioglass[®] to crystallize, with $\text{Na}_2\text{CaSi}_2\text{O}_6$ being the primary crystalline phase at this temperature [50]. The minimum $\text{Na}_2\text{Ca}_2\text{Si}_3\text{O}_9$ peaks appear at 550 °C, with $\text{Na}_2\text{CaSi}_2\text{O}_6$ as the secondary phase. Increasing the sintering temperature to 750 °C enhances the crystalline phase, with combeite $\text{Na}_2\text{Ca}_2\text{Si}_3\text{O}_9$ occurring as the sole crystalline phase in BG750. Conversely, when changing the fabrication method from sol-gel to melting and increasing the sintering temperature to 1400 °C, the quantity of combeite $\text{Na}_2\text{Ca}_2\text{Si}_3\text{O}_9$ decreases, and ($\text{Na}_2\text{Ca}_4(\text{PO}_4)_2\text{SiO}_4$) is detected as a secondary phase in the system [50].

The bioactivity and mechanical properties of bioactive glass can be tailored to meet the specific requirements of applications such as bone scaffolds. Increasing the crystallinity of the glass structure improves its mechanical properties, which is determined by the amount of combeite crystal formed during the synthesis process [36]. Table 4 displays the crystallinity data of combeite $\text{Na}_2\text{Ca}_2\text{Si}_3\text{O}_9$ for each tested sample. The mentioned crystallinity degree only applies to the combeite phase, and the actual combeite

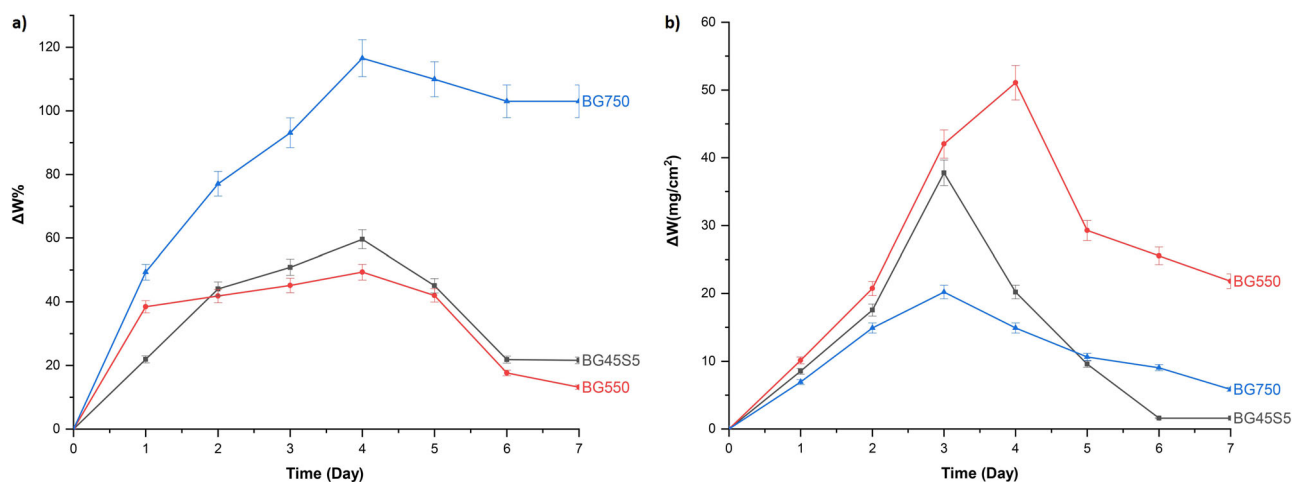


Fig. 5 a Swelling (b) Water Solubility Profiles of All Bioactive glass Samples. Statistical tests used were a One-way ANOVA with Holm-Bonferroni post-hoc ($n = 3$)

crystallinity values are given relative to 45S5 Bioglass[®]. The main variations in the crystallinity profiles of the samples are observed between the melting method and the sol-gel-derived method. BG750 exhibits higher crystallinity compared to BG550 and 45S5 Bioglass[®].

Table 4 shows the significant difference in crystallite size of combeite $\text{Na}_2\text{Ca}_2\text{Si}_3\text{O}_9$ across various sintering temperatures. The results indicate that the crystallite size for all samples ranges between 8 and 39 nm. Previous studies have noted that the crystallite size reported for combeite crystals obtained from 45S5 Bioglass[®] through thermal treatment at temperatures from 650 to 800 °C aligns with the findings in BG750 [18, 36]. Furthermore, the tendency for surface crystallization in bioglass 45S5 is observed in less dense bioglass structures, while bulkier samples exhibit bulk crystallization [46]. This observation aligns seamlessly with our findings, where the occurrence of surface crystallization during sintering at 550 °C, as evidenced by the small crystalline size of BG550 (7 nm), results in the lowest density among all samples (0.61 g/cm^3). As the sintering temperature increases, there is a corresponding observed increase in the density of the samples, culminating in the highest density and lowest porosity observed in BG45S5 (1 g/cm^3 and 46%, respectively), which was fabricated using the melting method. The direct impact of the fabrication technique and sintering temperature on crystallinity and crystalline size is demonstrated in the BET results. This correlation is further substantiated by the porosity and density data, wherein BG750 exhibits the optimum density and crystalline size with the highest crystallinity, indicating efficient sintering and densification. Conversely, BG550, with its smaller crystalline size and lower density, aligns with the characteristic of surface crystallization. The XRD and BET analyses and porosity and density measurements comprehensively understand the interplay between

fabrication conditions and the resultant crystalline structure. Such insights are invaluable for tailoring the properties of bioglass to specific biomedical applications, particularly in bone regeneration, where the balance of bioactivity and mechanical strength is essential.

3.6 Water intake properties

Investigating water intake and uptake in bioglasses is critical for enhancing their durability, particularly by developing bioglasses that are less prone to degradation by water molecules while retaining high mechanical strength [18]. Water uptake involves diffusion until saturation, during which water molecules can disrupt the network connectivity by dissociating Si-O-Si and P-O-Si linkages into hydroxyl groups [51, 52].

As shown in Fig. 5, swelling and solubility tests were conducted to evaluate the water absorption capacity of the bioglass samples. All samples demonstrated a tendency for linear water absorption throughout the experiment. BG750 showed a distinctive swelling behavior, with its highest water intake occurring on day 4, suggesting a more open network likely due to its increased crystallinity. Subsequently, the water intake rate decreased towards day 7. The BG750 sample's significant swelling could indicate its mesoporous structure, typical for sol-gel-derived bioglasses and advantageous for cell attachment and proliferation in bone scaffolds [53, 54]. The water intake rates for BG45S5, BG550, and BG750 were 9.42, 2.71, and 16.79% per day, respectively, with the release rates being 12.67, 12.05, and 4.5% per day, respectively. The imbalance observed in BG750's water intake and release rates reflects its unique structural properties. Notably, the average weight loss over seven days was minimal for all samples, indicating a resistance to mass loss in aqueous environments. This

suggests that the crystalline structure within BG750 may contribute to its stability and lower degradation rate in the presence of water [52].

The sol-gel method, known to create mesoporous textures and high surface areas, allows for better adsorption of biomolecules. This feature makes sol-gel-derived bioglasses attractive for biomedical applications where rapid *in vivo* resorption is desired. The high porosity, likely due to the crystalline phases within the sol-gel-derived bioglass, limits the material's compaction and facilitates its function in applications that benefit from faster resorption and integration with the host tissue [55].

3.7 Mechanical properties

The mechanical properties of bioglasses, specifically Young's modulus and compressive strength, are critical factors influenced by their crystallinity. The mechanical properties, specifically Young's (elastic) modulus and compressive strength, were determined from the collected stress-strain curves. The slope of the stress-strain curve provides Young's modulus [56]. Figures 6b, c depict the elastic modulus and compressive strength, respectively. The compressive stress-strain curve illustrates the elastic behavior of the samples under applied compressive force. The specimens undergo elastic deformation to store energy while resisting the applied force. Energy dissipation occurs within the internal network structure of the samples [44, 56, 57].

BG45S5, with lower crystallinity, showed the highest compressive strain value, deforming up to 58% under compressive stress exceeding 4 MPa (Fig. 6a). BG550 and BG750, with increasing crystallinity, exhibited lower compressive strains of 40 and 35%, respectively. The microstructural pore network, resulting from different fabrication methods and sintering temperatures, plays a pivotal role in this behavior. Higher crystallinity within BG750, as evidenced by XRD analysis, contributes to a denser network with reduced deformability under compressive loads [58].

Figure 7b highlights the compressive strength values with BG45S5 at the peak, having a strength of 5.35 MPa, which indicates less crystalline content, providing more deformability before failure. In contrast, BG750's compressive strength, while lower than BG45S5, is significantly higher than that of BG550, reflecting the structural impact of increased crystallinity due to higher sintering temperatures [44]. This increased porosity is correlated with higher crystallinity, which can enhance the mechanical strength to some extent; however, excessive crystallization can lead to brittleness, offsetting these gains [18, 46, 57]. The compressive strength of highly porous and biodegradable scaffolds, often studied as replacements for cancellous bone, typically falls within the range of 0.015 to 1 MPa [44].

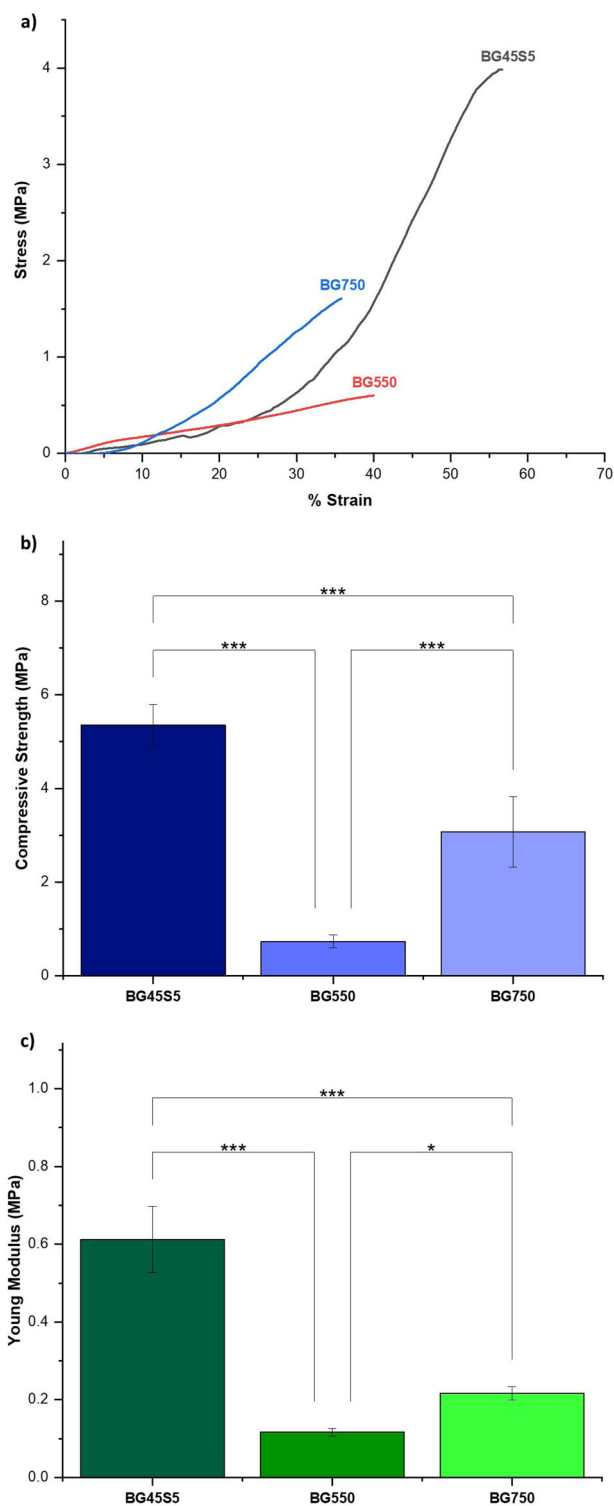


Fig. 6 a Stress- Strain behavior (b) Compressive Strength (c) Young Modulus of the Samples. ($n = 4$). Statistical tests used were a One-way ANOVA with Holm-Bonferroni post-hoc. Values are means \pm s.d. for three independent replicates. * $P \leq 0.05$ and *** $P \leq 0.001$

Furthermore, the compressive stress values for BG45S5 and BG750 fall within the range of compressive stress for cancellous and trabecular bone (1.5–45 MPa [50, 59]). good

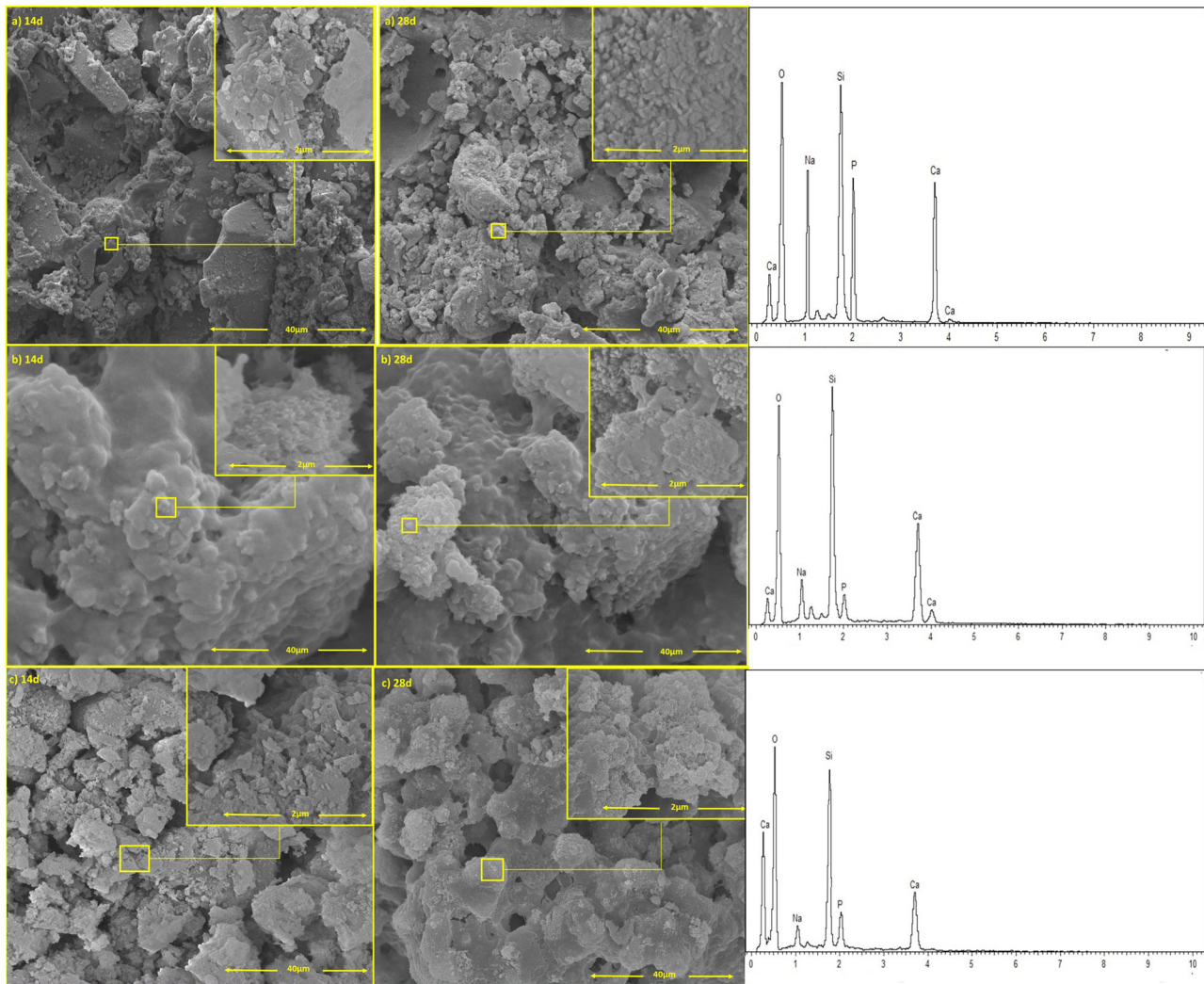


Fig. 7 FESEM images of no SBF refreshment (R-Samples) **(a)** BG45S5, **(b)** BG550, and **(c)** BG750

match between the scaffold's stiffness and the host tissue's stiffness enables effective stress transfer along the interface zone, leading to stable bonding and osteointegration [50].

The Young's modulus data presented in Fig. 7c show a general trend of decreasing modulus with increasing porosity [58] which aligns with the observed increase in crystallinity. BG45S5 exhibited the highest modulus, while BG750 showed a reduced modulus due to its higher porosity and crystallinity, highlighting the complex interplay between crystallinity, porosity, and mechanical performance [46, 50, 60]. These findings illuminate the nuanced relationship between crystallinity, porosity, and mechanical integrity in bioglasses. While a certain degree of crystallinity may reinforce the scaffold's mechanical strength, excessive crystallization can induce brittleness and compromise the mechanical properties. This balance is especially pertinent for scaffolds intended as cancellous bone replacements, where the mechanical properties should

mimic that of the surrounding bone to ensure effective stress transfer and osteointegration [45, 60, 61].

3.8 In vitro biomineralization study

3.8.1 Morphology

The bioactivity of bioactive glasses is significantly influenced by their surface interaction with physiological fluids, leading to the formation of a hydroxyapatite (HA) layer crucial for bonding with collagen filaments in the bone matrix. The crystallinity introduced by thermal treatment plays a key role in determining the surface morphology and subsequent bioactivity of these materials [44]. The in vitro bioactivity of the samples was confirmed by the formation of hydroxyapatite on the surface after immersion in SBF solution at 37 °C for 1, 7, 14, 21, and 28 days in both the melting and sol-gel bioglass preparations [17]. FESEM

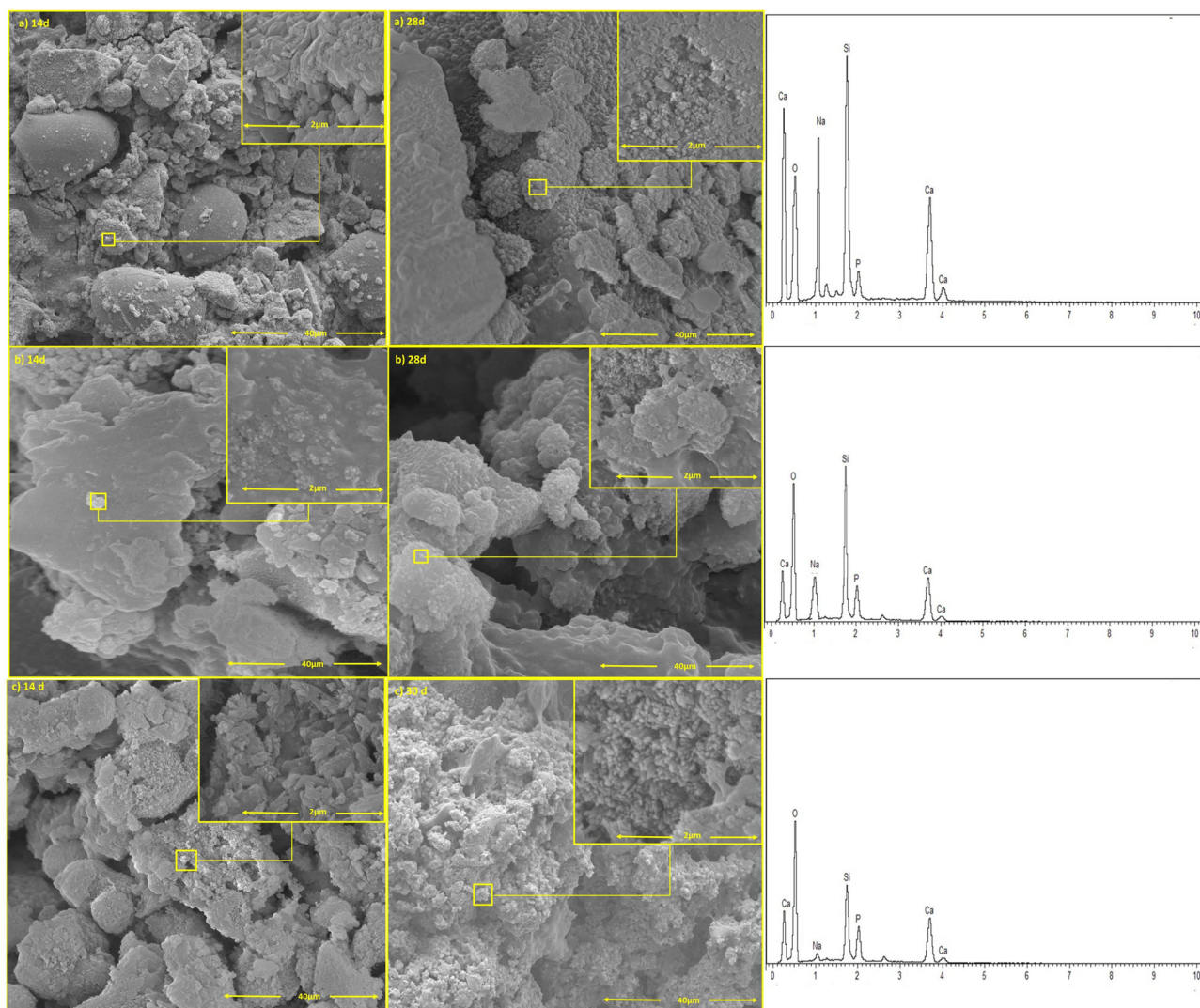


Fig. 8 FESEM images of SBF refreshment (NR-Samples) (a) BG45S5, (b) BG550, and (c) BG750

images of the surface of all bioglass samples were used to assess hydroxyapatite formation. Figures 7 and 8 depict the results, illustrating the formation of an apatite layer.

The mineralization process can be divided into nucleation and growth [50]. It is worth noting that the apatite crystals exhibit different morphologies during these two stages. Overall, the morphology of hydroxyapatite evolves from a needle-like shape to a worm-like layer, then fragments, and finally converges into a spherical shape after 28 days [7, 61]. The initial formation of HA crystal nuclei occurs at the corners of cracks. The ion exchange reaction between Ca^{2+} ions in the bioglass network and H^+ ions in the SBF solution readily takes place at the intersections of cracks. The water (H_2O) dissolves the Si-O bonds in the bioglass network, forming a porous silica gel layer on the material's surface, which contains a high concentration of $\equiv\text{Si-OH}$ groups. The OH^- groups in the SBF solution are

strongly attracted to the Ca^{2+} , H_2PO_4^- , and PO_4^{3-} ions, and the crack intersections provide ideal nucleation sites for hydroxyapatite [62, 63]. The needle-like structures exhibit as the typical morphology of HA formed on the silicate bioglasses after immersion in SBF [64].

Melt-derived 45S5 bioglass particles exhibit minimal surface porosity, low intrinsic roughness, and a smaller surface area compared to sol-gel bioglasses. Finer sol-gel bioglass particles have a higher surface area, promoting greater surface hydroxylation and the formation of a silica-rich gel layer (SiOH) compared to the 45S5 melt-derived glasses. The silica-rich gel layer in sol-gel bioglass provides more sites for the nucleation of the calcium phosphate (the precursor to apatite) layer [55].

After 14 days of immersion in SBF solution, both groups showed the accumulation of inhomogeneous hydroxyapatite nanoparticles with cracks on their surfaces. Minor cracks

and hydroxyapatite particles were observed on BG550 in both groups. These microcracks indicate that the particles composing all the bioglass samples were heterogeneous, allowing for stress concentration. Additionally, the samples experienced swelling after immersion in SBF solution, resulting in cracks due to the combined physical and chemical reactions between the bioglass surface and the SBF solution through water erosion and ion exchange. As the density of the mineralization layer increased, the growth of hydroxyapatite crystals gradually covered the microcracks. The PO_4^{3-} and Ca^{2+} ions in all samples diffused into the SBF solution through the porous silica gel layer, causing ionic supersaturation in the solution and the formation of water-rich $\text{CaO-P}_2\text{O}_5$ sediments that covered the silica gel layer [63]. The bioactivity of a biomaterial is believed to be closely related to the speed of mineral deposition, with higher bioactivity associated with rapid deposition [65]. The observation that all bioglass samples exhibited incomplete coverage of the surface with sphere-shaped HA crystals after 28 days of immersion in SBF at a constant pH (Fig. 7a, b, c) indicates that the HA layer was not dense and stable, which is further confirmed by subsequent XRD results. Meanwhile, after 28 days, well-developed spherical crystals were distributed on the surfaces of BG45S5 and BG750, with many small agglomerations visible. However, minimal distribution was observed on the surface of BG550 (Fig. 7b). On the other hand, when the pH was not constant (NR-Samples), BG750 exhibited a more homogeneous surface without cracks compared to the other NR-Samples (Fig. 8a, c). This indicates that BG750 allows for effortless stress concentration. In general, the sintering temperature directly affects the bioactivity of the bioglass.

The EDX analysis, following 28-day immersion in SBF, confirmed the development of apatite with bone-like characteristics in both the melting and sol-gel bioglasses. Figures 7 and 8 show the detection of peaks corresponding to Si, P, Ca, Na, and O. The deposition of Ca and P ions on a glass surface over time has been observed to promote favorable activities related to bone formation. All synthesized glasses exhibited susceptibility to biomineralization, and the surfaces of the bioglasses were reactivated in terms of the formation of calcium- and phosphorus-rich layers. The preferential interaction of Ca^{2+} with non-bonding oxygens from phosphates, as opposed to silicates, suggests that an increase in the number of phosphate units within the bioglass structure would hinder the migration kinetics of Ca^{2+} toward the bioglass surface, thereby promoting the development of a layer with a calcium-deficient composition [66].

According to the EDX analysis, Table 5 presents the Ca/P molar ratios of the bone-like apatite in both groups. As per previous literature, the theoretical Ca/P ratio of HA is 1.67 [66–68]. The texture of sol-gel bioglass can be varied by manipulating distinct processing parameters, including pH,

Table 5 Ca/P ratio of HA layer formation after 28 days immersion in SBF solution

Ca/P Ratio		
Sample Name	NR- Samples	R- Samples
BG45S5	1.63	1.58
BG550	1.55	1.25
BG750	1.65	1.62

reagent concentrations, stabilization temperature, and drying conditions [55]. As a result, sol-gel samples provide more nucleation sites for the calcium phosphate layer, which serves as the precursor to apatite. Moreover, by increasing the sintering temperature from 550 to 750 °C, BG750 exhibited higher bioactivity and Ca/P ratio than BG550. Based on the FESEM investigation and EDX analysis, BG750 demonstrated promising bioactivity after 28 days of immersion in SBF solution.

The intricate relationship between morphology, crystallinity, and bioactivity highlights the importance of optimizing thermal treatment to balance these factors effectively. As the sintering temperature increases, crystallinity is enhanced, improving bioactivity. However, an excess of crystalline phases, particularly secondary phases like $(\text{Na}_2\text{Ca}_4(\text{PO}_4)_2\text{SiO}_4)$, can potentially restrict the bioactivity and uniformity of the HA layer, affecting the material's suitability for biomedical applications such as bone scaffold implants (Mecca 2023 and 48). These findings from the FESEM and EDX analyses highlight the significance of crystallinity in tailoring the morphology and bioactivity of bioactive glasses. BG750, with its higher crystallinity achieved through optimal sintering, emerges as a promising candidate for biomedical applications due to its superior bioactivity and the formation of an HA layer with a favorable Ca/P ratio after 28 days of immersion in SBF.

3.8.2 Evaluation of pH values and ion concentration

The bioactivity of biomaterials in SBF is often assessed through the pH profile and ion concentration measurements, both indicative of the materials' surface reactions. Initially, all porous scaffolds exhibit a surge in pH due to the rapid ion exchange between alkaline and alkaline earth ions from the bioglass with the H^+ ions in the SBF solution, releasing Ca^{2+} and potentially forming hydroxyl groups which contribute to the initial layer of hydroxyapatite [69–72]. After the first day, the pH steadily rose by releasing Ca^{2+} into the medium to form a $\text{CaO-P}_2\text{O}_5$ -rich layer on the surface of the bioglass. This ion exchange generates hydroxyl groups, which are responsible for the formation of the hydroxyapatite layer. Subsequently, the pH gradually increased as Ca^{2+} was released into the medium, leading to the

formation of a CaO–P₂O₅-rich layer on the bioglass surface. The required calcium for hydroxyapatite formation on the silica gel surface was obtained from the SBF. This is supported by observing a decrease in calcium concentration in the solution [71, 73]. Over time, some calcium ions also contributed to developing the HA layer [69, 73]. However, the supply of calcium from the bulk material was insufficient to sustain the growth of the HA layer, resulting in a maximum calcium concentration being reached [73].

Figure 9a and Table 6 illustrates the pH variation of NR-Samples during the immersion period. The pH variation (Δ pH) for BG45S5, BG550, and BG750 was 0.65, 0.69, and 0.71, respectively. The pH values exhibited a rapid increase within the first day, followed by different trends in each sample. Notably, for BG45S5, the pH steadily decreased until day 14, likely due to its higher porosity and lower surface area, leading to distinct ion release kinetics that influenced the degradation rate. For BG550 and BG750, the pH initially dropped on day 7 and then gradually rose over the next three weeks. This pH variation is undoubtedly influenced by changes in Ca ion concentration. The data from Table 6 show that the pH values after 28 days for BG45S5, BG550, and BG750 were 7.89, 8.04, and 8.00, respectively, indicating a stabilization phase towards the end of the immersion period. Moreover, this fluctuation may be associated with the different degrees of crystallinity observed in BG45S5, BG550, and BG750. The higher crystallinity in BG750, as evidenced by the XRD results, suggests a slower ion exchange rate due to a more ordered structure, which could explain the more stable pH profile compared to BG550 and BG45S5 [71, 73, 74].

Figure 9b shows the Ca ion concentration profiles for all NR-Samples. The profile of Ca ion concentration aligns with the pH behavior. Bioglass particles, which generally have a disordered atomic arrangement (amorphous), release ions from the bioglass structure more quickly than the crystalline particles [74]. The pH and Ca concentration profiles of NR-Samples indicate that BG750 exhibited the highest rate of change without significant fluctuations. This observation may be attributed to the influence of morphology and porosity from the sol-gel technique's sintering temperature [58]. This profile evaluation could be explained by the increased surface area of the samples due to the calcination temperature, which is responsible for increasing the porosity and permeability of the sample [69]. The observed pH variation is likely to occur in new tissue constructs both in vitro and in vivo [75].

Figure 9c displays the Ca concentration profiles of R-Samples. All bioglasses in R-Samples groups exhibited approximately 60 mg/L of Ca concentration on the first day. However, different behavior was observed between melting and sol-gel bioglasses from day 7 to day 28. During this period, the Ca concentration of BG550 and

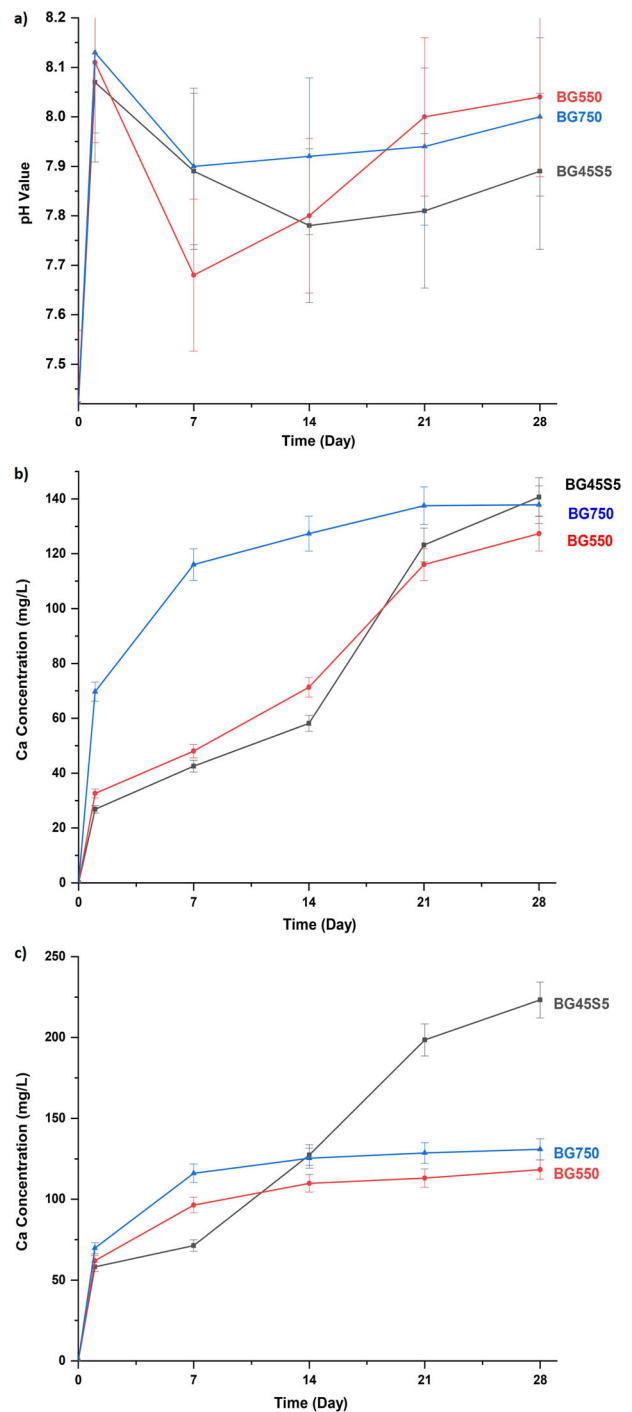
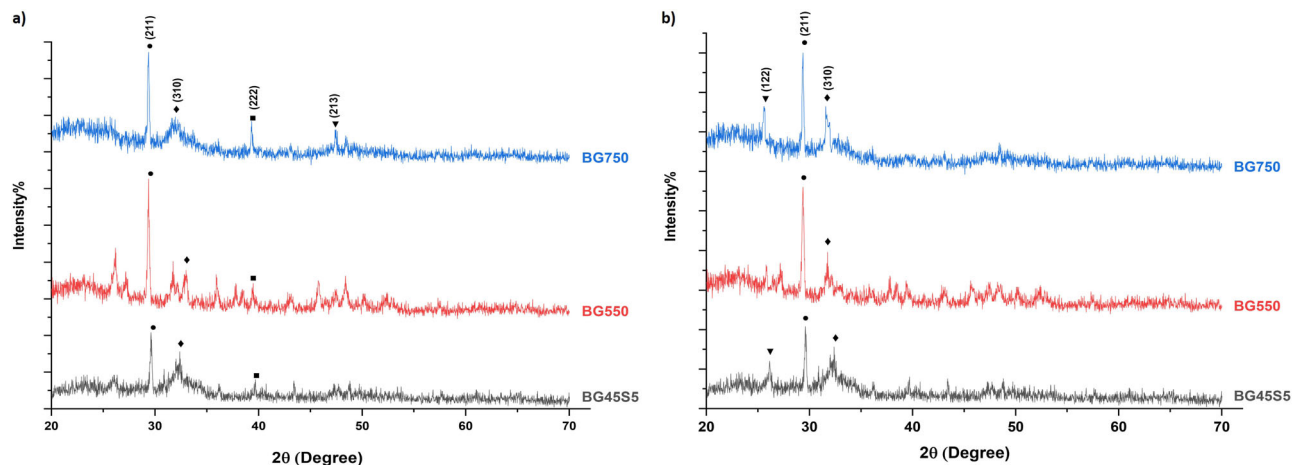


Fig. 9 a pH evaluations profile (b) Ca concentration of NR-Samples (c) Ca concentration of R-Samples after immersion in SBF within 28 days

BG750 remained relatively stable with minimal fluctuations, while BG45S5 exhibited a similar trend in both groups. These results indicate that, under constant pH conditions, the diffusion of Ca²⁺ from the R-Samples group into the SBF solution was higher than the NR-Samples. The XRD results also support the notion that a

Table 6 pH values and Ca concentration of samples after 28 days immersion in SBF solution

Day	pH Value			Ca concentration (mg/L)					
	BG45S5	BG550	BG750	NR- Samples			R- Samples		
				BG45S5	BG550	BG750	BG45S5	BG550	BG750
0	7.42	7.42	7.42	0	0	0	0	0	0
1	8.07	8.11	8.13	26.81	32.59	69.72	58.17	61.96	69.72
7	7.89	7.68	7.90	42.51	48.02	116.02	71.32	96.33	116.02
14	7.78	7.80	7.92	58.17	71.32	127.35	127.35	109.85	125.35
21	7.81	8.00	7.94	123.20	116.02	137.55	198.53	113.05	128.55
28	7.89	8.04	8.00	140.68	127.35	137.88	223.20	118.26	130.88

**Fig. 10** X-ray diffraction diffractograms of all bioglass samples incubated in simulated body fluid for 28 days (a) without refreshment (NR-Samples), (b) with constant pH (R-Samples)

constant pH increases the tendency of bioglass to form a CaO–P₂O₅-rich layer at the interface. However, it does not allow for forming a thick and stable HA layer within 28 days. While the pH change results indicate the release of ions, particularly Ca²⁺, into the SBF solution, the degradation rate is a multifaceted process influenced by various parameters, such as porosity, crystallinity, and surface area. BG45S5, with higher porosity and lower surface area, exhibits distinct ion release kinetics, influencing the degradation rate. Furthermore, the crystallinity results indicate that BG750's higher crystallinity may impact mechanical properties and degradation behavior, potentially slowing down the degradation process. The interplay of these factors underscores the complex dynamics of ion release and bioactivity in bioglasses [73, 76].

3.8.3 Crystallinity analysis

Figure 10 illustrates the XRD results obtained from two groups of samples: NR-Sample and R-Sample. The comparison of these peaks with the Joint Committee on Powder Diffraction Standards (JCPDS #09-0432) revealed that both

sample groups exhibited HA layers within the 20 to 70 range. In both groups, the diffraction peaks at $2\theta = 24, 29,$ and 32 corresponded to the (211) and (310) reflections of HA crystals. Additionally, the NR-samples group demonstrated the most robust and most stable diffraction peaks at $2\theta = 39$ and 49 , which corresponded to the (222) and (213) reflections of HA, respectively (BG750 showed the (213) reflection exclusively) [70, 77, 78].

The formation of hydroxyapatite did not strictly adhere to favorable stoichiometric conditions. Under low pH conditions, the interface of other precursors or the amorphous HA phase formed, leading to apatite formation. A constant pH of 7.42 presented a complex situation where other ions or molecules could be present within the crystalline lattice or on its surface. As mentioned before, acidic conditions favored the reaction that stoichiometrically formed the monoclinic phase, stabilizing the hydroxyapatite structure expected in bone tissue [78–80]. Based on the XRD analysis and crystallinity data (Table 5), it was determined that the bioglass samples without refreshment exhibited a high level of in vitro bioactivity, with all bioglasses developing a HA layer within four weeks in the SBF solution. This observation was further confirmed by the FESEM images and EDX results associated with this group.

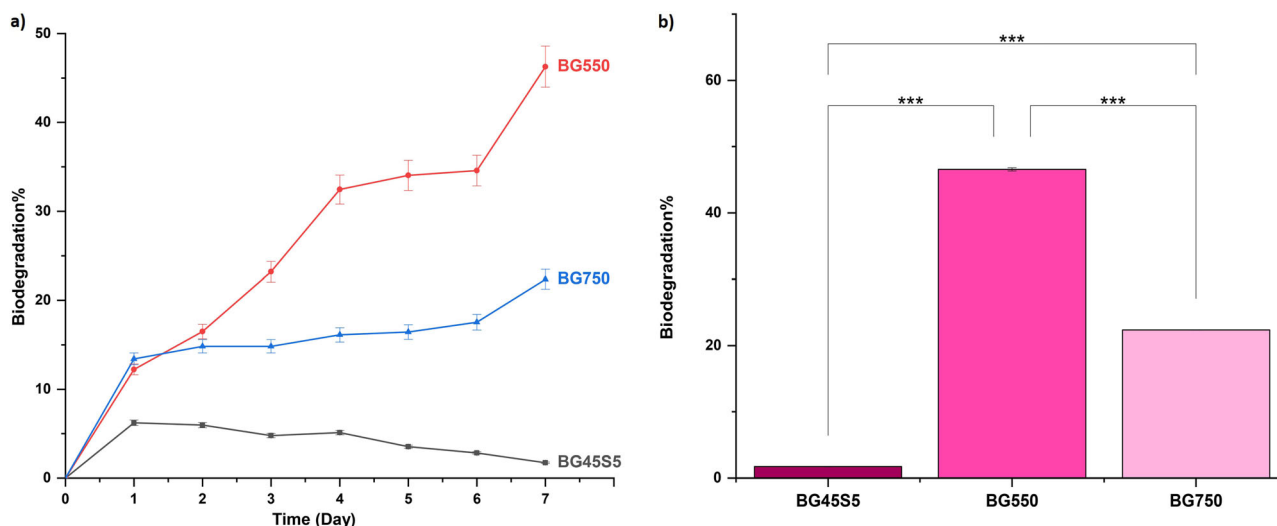


Fig. 11 **a** The biodegradation rate of bioglasses within 7 days. **b** The average of weight loss after 7 days. Statistical tests used were a One-way ANOVA with Holm-Bonferroni post-hoc ($n = 3$). Values are means \pm s.d. for three independent replicates. *** $P \leq 0.001$

However, the strong HA layer observed in the R-samples was not replicated. This suggests that rehydrating the SBF solution and maintaining a constant pH allow sufficient time for the transformation from initial mineralization deposition to the formation of a robust and dense HA layer [78].

3.8.4 In vitro degradation study

The degradability of scaffolds is crucial for their function in tissue engineering. Ideally, scaffolds should degrade at a rate that matches host tissue regeneration. The in vitro degradation behavior of bioactive glasses is influenced by factors such as molecular weight, crystallinity, and porosity [81]. Bioactive glasses are designed to be absorbed by the body, with resorbed glass replaced by regenerated bone. Upon contact with body fluids, these glasses undergo a series of reactions that break bonds between network formers like Si or P and oxygen, leading to the dissolution of the glass and subsequent bone tissue formation [18].

Figure 11b displays the bioglass weight loss after a one-week incubation in PBS at pH 7.4. After this period, approximately 2, 46, and 23% degradation were observed for BG45S5, BG550, and BG750, respectively. An increase in calcination temperature during the sintering of bioglass is known to enhance chemical stability and moderate the degradation rate, which may be associated with reduced porosity and increased crystallinity at higher temperatures [58, 81]. The higher porosity observed in the BG750 network is conducive to a more extensive breakdown of the bioglass structure compared to BG45S5. At the same time, BG550 exhibits the most rapid degradation rate, potentially due to its lower crystallinity, which enhances its solubility and ion exchange in physiological environments [81].

Figure 11b displays the weight loss of all samples after one week of incubation in PBS at pH 7.4. After seven days, approximately 2, 46, and 23% of BG45S5, BG550, and BG750, respectively, had undergone degradation. Increasing the calcination temperature during bioglass sintering enhanced the chemical stability and degradation rate across all time points. This effect could be associated with increased porosity, as the porosity decreased with an increase in temperature from 750 to 1400 °C [58]. The balance between crystallinity and porosity is critical in dictating the degradation rate of bioactive glasses. While porosity typically increases degradation due to a larger reactive surface area, crystallinity introduced by higher sintering temperatures can stabilize the structure and slow down the degradation process. The need to finely adjust these parameters is essential to achieve the desired degradation rate for bioactive glass scaffolds in bone tissue engineering [18, 82].

3.9 In vitro antibacterial evaluation

The antibacterial properties of bioactive glasses like Bioglass 45S5 are multifaceted, originating from the local increase in pH, elevated osmotic pressure, and potential mechanical damage to bacterial cell walls from the glass particulates. These factors can collectively lead to bacterial cell death upon contact with the glass materials [67, 83–85]. Notably, the optimal growth pH for most bacteria is near neutral; thus, an alkaline shift can hinder their proliferation. The dissolution of bioactive glasses releases ions such as Ca^{2+} , Si^{4+} , Na^+ , and PO_4^{3-} , which can disrupt the bacterial membrane potential and contribute to an inhospitable environment [71, 84, 86]. Figure 12 shows the antibacterial

efficacy of various bioglass samples against both Gram-negative *E. coli* and Gram-positive *S. aureus*, with Table 7 detailing the pH changes experienced by these strains during exposure to the bioglasses. The bactericidal effects, shown in Figs. 12a, b, indicate a pronounced inhibitory action on *E. coli*, which exhibits greater sensitivity to the bioglasses than *S. aureus*. This differential susceptibility may be related to the unique growth dynamics and cell wall composition of these bacterial species [44, 87].

As discussed in “Crystallinity Analysis” and evidenced by the XRD results, the sintering temperature, which affects the crystalline size, determines antibacterial activity. Smaller crystalline, resulting from lower sintering temperatures, present a larger surface area for interaction with bacteria, potentially facilitating the release of more ions into the environment. This can lead to a higher pH and osmotic pressure, which is detrimental to bacterial viability [71, 84, 86]. Among the tested samples, BG750 is the most effective against *E. coli*, showing a notable difference in inhibition compared to BG550. As per the findings in “Evaluation of pH values and Ion concentration”, BG750 demonstrates an elevated release of Ca^{2+} ions, whereas BG550 has the lowest ion release profile, correlating with their respective antibacterial activities. The release of Ca^{2+} ions from BG750 significantly reduces the viability of both

E. coli and *S. aureus*, endorsing its potential for applications in bone tissue engineering. Table 7 presents the pH changes during the antibacterial tests, further supporting the idea that releasing bioactive ions from the glasses contributes to increased environmental pH, which is inhospitable to the bacteria tested.

The antibacterial properties are significantly influenced by the degradation rate, crystallinity, and ion release profiles of the bioglass samples. BG750, which was sintered at a higher temperature, exhibited higher crystallinity and a slower ion exchange rate, leading to more stable pH profiles compared to BG550 and BG45S5. This stability enhances the antibacterial efficacy by maintaining an uninhabitable environment for bacterial growth. The degradation rate of the bioglass, which is faster in less crystalline samples like BG550, also plays a crucial role in the antibacterial activity in which faster degradation indicates lower bacterial resistance of the produced bioglass. The increased porosity and permeability of BG750 also contribute to a better ion release; hence, enhance its antibacterial properties and support its potential use in bone tissue engineering applications.

3.10 In vitro biological evaluation

Cytocompatibility is a vital aspect of bioactive materials' assessment, where cell viability acts as a primary indicator of material suitability for biomedical applications [18]. The MTT assay, which quantitatively evaluates cell adhesion and proliferation, was utilized to determine the viability of MC3T3 cells exposed to 24-h extracts of bioglass powders. For a material to be conducive to tissue regeneration, it should support cellular activities and be inherently non-toxic [54]. A viability percentage above 70% is generally accepted as a benchmark for non-toxicity, while values

Table 7 pH changes during bacteria inhibition

Sample Name	<i>E. coli</i>		<i>S. aureus</i>	
	Initial pH	Final pH	Initial pH	Final pH
BG45S5	6.71 ± 0.22	8.96 ± 0.22	6.75 ± 0.10	9.20 ± 0.29
BG550	6.71 ± 0.22	8.39 ± 0.11	6.75 ± 0.10	8.95 ± 0.21
BG750	6.71 ± 0.22	9.76 ± 0.14	6.75 ± 0.10	9.76 ± 0.18

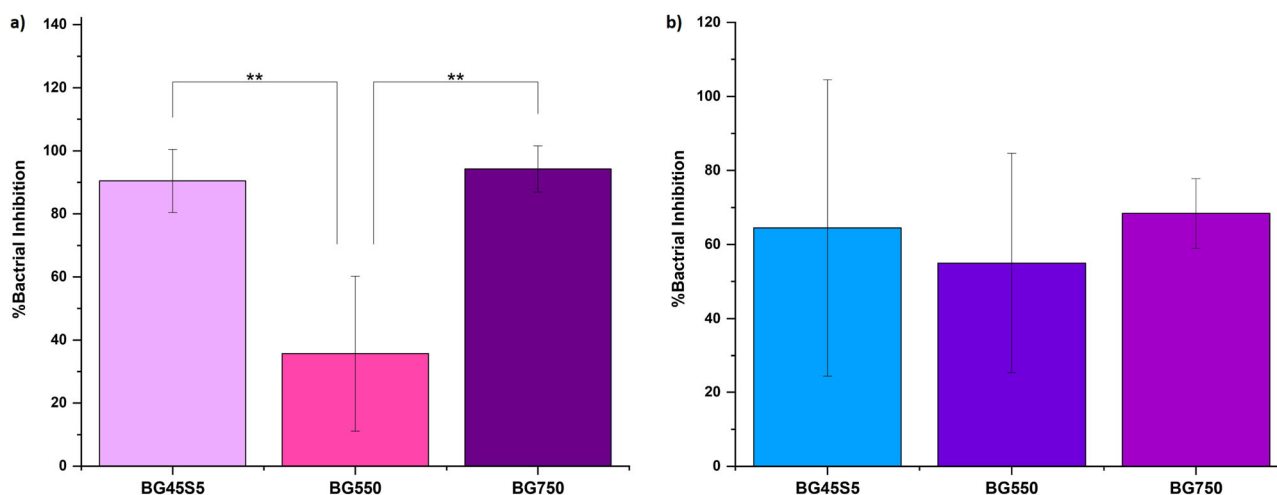


Fig. 12 Bacterial inhibition of (a) *E. coli*, (b) *S. aureus* ($n = 3$). Statistical tests used were a One-way ANOVA with Holm-Bonferroni post-hoc. Values are means ± s.d. for three independent replicates. $P \leq 0.01$

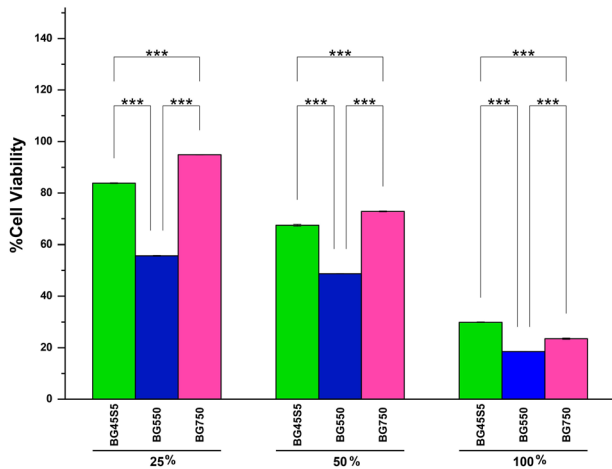


Fig. 13 Percentage viability of MC3T3 cultured with 25, 50, and 100% extraction of bioglass samples in 24 h. Statistical tests used were a One-way ANOVA with Holm-Bonferroni post-hoc. Values are means \pm s.d. for three independent replicates. $P \leq 0.001$

below this indicate potential cytotoxicity [64, 88]. The outcomes of the viability assays are presented in Fig. 13.

The MTT assay results revealed that the MC3T3 cells cultured with the sol-gel-derived bioglass sintered at 750 °C exhibited a level of viability on par with those cultured with the melt-derived BG45S5, both demonstrating high cell viability ($P < 0.001$). An increase in metabolic activity was observed with a 25% extract from all bioglass types, suggesting a favorable environment for cell proliferation ($P < 0.001$). The selection of a 25% extract for these studies was based on protocols designed to reduce assay interference while maintaining assay sensitivity [18, 64, 88]. The absence of a phosphorus peak in BG550's EDX spectrum (Fig. 3b) indicates a deficiency in forming a bioactive phosphorus-rich layer at this sintering temperature, which is vital for promoting cell viability. Additionally, the ion release and pH profiles discussed in "Evaluation of pH values and Ion concentration" reveal how BG550's fluctuating pH and ion dissolution dynamics can negatively interact with the cellular environment. The pH profile for BG550 showed an initial disturbance followed by a steady increase, leading to the highest pH observed on day 21 among all bioglass samples. This unstable behavior is corroborated by the FESEM and EDX findings, suggesting that the leaching of BG550's material components may have created an alkaline milieu detrimental to cell viability. Such leaching could be responsible for the near absence of viability in BG550 at the 25% extract concentration, exposing the cells to a potentially cytotoxic environment [18, 54, 64, 88]. These results highlight the significance of a holistic evaluation encompassing both the biological response and the physicochemical characteristics of bioactive glasses. The evidence suggests that bioglass scaffolds synthesized via the sol-gel method and sintered at 750 °C

are well-suited for bone grafting applications due to their stable physicochemical properties and their promotion of a biologically favorable environment for cellular growth.

4 Conclusion

In comparison to commercial bioactive glasses like 45S5, which exhibit extremely narrow sintering windows, making them challenging to subject to thermal treatment without inducing crystallization, this study delves into the effects of sintering temperature on bioglasses synthesized using both melting and sol-gel techniques. Recognizing the limitations posed by the narrow sintering windows of commercial bioactive glasses, researchers have endeavored to explore new BG compositions or modify existing ones to achieve glasses with broader sintering windows, with the primary aim of enabling successful sintering while mitigating the crystallization process. This study comprehensively examines the effects of sintering temperature on bioglasses synthesized using melting and sol-gel techniques. The findings highlight significant distinctions between the bioglasses obtained through these two methods at various sintering temperatures. The commercial 45S5 bioglass demonstrated remarkable stability, as confirmed by TGA/DSC analysis compared to the sol-gel bioglasses. The FTIR analysis further indicated that BG750 exhibited the highest number of oxygen bonds, suggesting a distinctive chemical composition. Morphology analysis revealed distinct characteristics, with BG45S5 displaying an intrinsic rough fracture surface, BG550 exhibiting non-porous surfaces, and BG750 showing a well-defined, porous, interconnecting structure with 5.459 m²/g of surface area, 0.217 cm³/g (total pore volume) and 79.50 nm pore size. Crystallinity analysis indicated the formation of combeite Na₂Ca₂Si₃O₉ as the sole crystalline phase in BG750. Mechanical properties demonstrated that BG45S5 had the highest compressive strength (3.5 MPa). In comparison, sol-gel bioglasses sintered at 750 °C exhibited improved modulus with a trade-off in macroporous structure compared to BG550 (0.22 and 0.12 MPa, respectively). The antibacterial evaluation demonstrated inhibitory effects on both gram-negative and gram-positive bacteria, with the sintering temperature influencing the antibacterial activity. The in vitro biological evaluation using MC3T3 cells indicated the biocompatibility and proliferative potential of all bioglass samples, with sol-gel bioglasses stabilized at 750 °C exhibiting comparable viability to the commercially established 45S5 bioglass.

Overall, the sol-gel bioglass synthesized at 750 °C exhibited distinct characteristics, including higher crystallinity, oxygen bond content, and calcium ion release, as well as enhanced biocompatibility and mechanical

properties. These findings highlight the potential of utilizing sol-gel bioglass synthesized at 750 °C for bone grafting and tissue engineering applications. However, further research is imperative to optimize its performance, specifically in load-bearing sites and to ensure its suitability for clinical implementation.

Acknowledgements The work was funded by Universiti Putra Malaysia under Geran Putra Inisiatif Siswazah (9669500). All chemical analyses were conducted at the Material Characterization Laboratory, Faculty of Engineering, Universiti Putra Malaysia. The sintering processes and microscopic analyses were performed at the Institute of Nanomaterial and Nanotechnology, Universiti Putra Malaysia. The biological analysis was conducted at the Cancer Research Laboratory, Institute of Bioscience, Universiti Putra Malaysia.

Author contributions M Sarmast Sh: Writing – original draft, Software, Methodology, Investigation, Formal analysis, Data curation. AB Dayang Radiah: Supervision of project, Writing – review & editing, Funding acquisition. D. A. Hoey: Writing – review & editing, Validation, Funding acquisition, Formal analysis. N Abdullah: Investigation and methodology H S Zainuddin: Investigation and Editing. S Kamarudin: Methodology and Validation.

Compliance with ethical standards

Conflict of interest The authors declare no competing interests.

References

- Deshmukh K, Kovářík T, Křenek T, Docheva D, Stich T, Pola J (2020) Recent advances and future perspectives of sol-gel derived porous bioactive glasses: a review. *RSC Advances* 10(56 Sep):33782–33835. <https://doi.org/10.1039/d0ra04287k>. Royal Society of Chemistry
- Baino F (2021) Bioactive glasses and glass-ceramics. In *Encyclopedia of materials: technical ceramics and glasses*, vol. 3–3, Elsevier, p 614–623. <https://doi.org/10.1016/B978-0-12-803581-8.12088-0>
- Jones JR (2015) Review of bioactive glass: from Hench to hybrids. *Acta Biomater* 23(S):S53–S82. <https://doi.org/10.1016/j.actbio.2015.07.019>
- Shoushtari MS, Hoey D, Biak DRA, Abdullah N, Kamarudin S, Zainuddin HS (2024) Sol-gel-templated bioactive glass scaffold: a review. *Res Biomed Eng*. <https://doi.org/10.1007/s42600-024-00342-x>
- Li R, Clark AE, Hench LL (1991) An investigation of bioactive glass powders by sol-gel processing. *J Appl Biomater* 2(4):231–239. <https://doi.org/10.1002/jab.770020403>
- Lei Q, Guo J, Noureddine A, Wang A, Wuttke S, Brinker CJ, Zhu W (2020) Sol-Gel-based advanced porous silica materials for biomedical applications. *Adv Function Mater*, 30 Wiley-VCH Verlag. <https://doi.org/10.1002/adfm.201909539>
- Bellucci D, Sola A, Salvatori R, Anesi A, Chiarini L, Cannillo V (2014) Sol-gel derived bioactive glasses with low tendency to crystallize: synthesis, post-sintering bioactivity and possible application for the production of porous scaffolds. *Mater Sci Eng C* 43(Oct):573–586. <https://doi.org/10.1016/j.msec.2014.07.037>
- Lefebvre L, Gremillard L, Chevalier J, Zenati R, Bernache-Assollant D (2008) Sintering behaviour of 45S5 bioactive glass. *Acta Biomater* 4(6):1894–1903. <https://doi.org/10.1016/j.actbio.2008.05.019>
- Chitra S, Bargavi P, Durgalakshmi D, Rajashree P, Balakumar S (2019) Role of sintering temperature dependent crystallization of bioactive glasses on erythrocyte and cytocompatibility. *Process Appl Ceramics* 13(1):12–23. <https://doi.org/10.2298/PAC1901012C>
- Bahniuk MS, Pirayesh H, Singh HD, Nychka JA, Unsworth LD (2012) Bioactive glass 45S5 powders: effect of synthesis route and resultant surface chemistry and crystallinity on protein adsorption from human plasma. *Biointerphases* 7(1–4):1–15. <https://doi.org/10.1007/s13758-012-0041-y>
- Pirayesh H, Nychka JA (2013) Sol-gel synthesis of bioactive glass-ceramic 45S5 and its in vitro dissolution and mineralization behavior. *J Am Ceramic Soc* 96(5 May):1643–1650. <https://doi.org/10.1111/jace.12190>
- Sepulveda P, Jones JR, Hench LL Bioactive sol-gel foams for tissue repair, [Online]. Available: <https://doi.org/10.1002/jbm.1250>
- Hench LL, Andersson Ö (1993) BIOACTIVE GLASSES. In *An Introduction to Bioceramics*. p 41–62. https://doi.org/10.1142/9789814317351_0003
- Tulyaganov DU et al. (2011) Synthesis, bioactivity and preliminary biocompatibility studies of glasses in the system CaO-MgO-SiO₂-Na₂O-P₂O₅-CaF₂. *J Mater Sci Mater Med* 22(2 Feb):217–227. <https://doi.org/10.1007/s10856-010-4203-5>
- Wang Z, Gao T, Cui L, Wang Y, Zhang P, Chen X (2016) Improved cellular infiltration into 3D interconnected microchannel scaffolds formed by using melt-spun sacrificial microfibers. *RSC Adv* 6(3):2131–2134. <https://doi.org/10.1039/C5RA25142G>
- International Organization for Standardization (ISO) (2014) ISO 23317:2014 Implants for surgery — In vitro evaluation for apatite-forming ability of implant materials, Technical Committee: ISO/TC 150/SC 1
- Kokubo T, Takadama H (2006) How useful is SBF in predicting in vivo bone bioactivity? *Biomaterials* 27(15):2907–2915. <https://doi.org/10.1016/j.biomaterials.2006.01.017>
- Bargavi P, Balakumar S, Raghunandhakumar S (2024) Multi-functional bandage - bioactive glass/metal oxides/alginate composites based regenerative membrane facilitating re-epithelialization in diabetic wounds with sustained drug delivery and anti-bactericidal efficacy. *Int J Biol Macromol* 262(Mar):130054. <https://doi.org/10.1016/J.IJBIOMAC.2024.130054>
- Mukundan LM, Nirmal R, Vaikkath D, Nair PD (2013) A new synthesis route to high surface area sol gel bioactive glass through alcohol washing: a preliminary study. *Biomater* 3(2):1–10. <https://doi.org/10.4161/biom.24288>
- Ciapetti G, Cenni E, Pratelli L, Pizzoferrato A (1993) In vitro evaluation of cell/biomaterial interaction by MTT assay. *Biomaterials* 14(5 Apr):359–364. [https://doi.org/10.1016/0142-9612\(93\)90055-7](https://doi.org/10.1016/0142-9612(93)90055-7)
- Wen C et al. (2021) Structural behavior and in vitro bioactivity evaluation of hydroxyapatite-like bioactive glass based on the SiO₂-CaO-P₂O₅ system. *Ceram Int* 47(13 Jul):18094–18104. <https://doi.org/10.1016/j.ceramint.2021.03.125>
- Khiri MZA et al. (2020) Soda lime silicate glass and clam Shell act as precursor in synthesize calcium fluoroaluminosilicate glass to fabricate glass ionomer cement with different ageing time. *J Mater Res Technol* 9(3):6125–6134. <https://doi.org/10.1016/j.jmrt.2020.04.015>
- Xue B et al. (2019) Sol-gel preparation of anti-bacterial and bioactive glass-ceramics. *J Biomater Appl* 34(1):86–93. <https://doi.org/10.1177/0885328219843901>
- Araujo A (2020) Structural and thermal behavior of 45S5 Bioglass®-based compositions containing alumina and strontium. *J Am Ceramic Soc* 103:3620–3630

25. Li A et al. (2017) Detailed structure of a new bioactive glass composition for the design of bone repair materials. *J Non-Cryst Solids* 475(Nov):10–14. <https://doi.org/10.1016/J.JNONCRY SOL.2017.07.027>
26. Haghghi FD, Beidokhti SM, Najaran ZT, Saghi SS (2021) Highly improved biological and mechanical features of bioglass-ceramic/gelatin composite scaffolds using a novel silica coverage. *Ceram Int*. <https://doi.org/10.1016/j.ceramint.2021.01.274>
27. Sohrabi M, Hesarakhi S, Kazemzadeh A, Alizadeh M (2013) Development of injectable biocomposites from hyaluronic acid and bioactive glass nano-particles obtained from different sol-gel routes. *Mater Sci Eng C* 33(7 Oct):3730–3744. <https://doi.org/10.1016/j.msec.2013.05.005>
28. Ibrahim NF, Mohamad H, Mohd Noor SNF, Ahmad N (2017) Apatite formation on melt-derived bioactive glass powder based on $\text{SiO}_2\text{-CaO-Na}_2\text{O-P}_2\text{O}_5$ system. *Ceram Int* 43(15):11676–11685. <https://doi.org/10.1016/j.ceramint.2017.05.356>
29. Borhan S, Hesarakhi S, Behnamghader AA, Ghasemi E (2016) Rheological evaluations and in vitro studies of injectable bioactive glass–polycaprolactone–sodium alginate composites. *J Mater Sci Mater Med* 27. <https://doi.org/10.1007/s10856-016-5745-y>.
30. Ismail N, Mohamad H, Ahmad N (2020) Fabrication and characterization of 45S5 bioactive glass microspheres. In *AIP Conference Proceedings*, American Institute of Physics Inc. <https://doi.org/10.1063/5.0015700>
31. Hum J, Boccaccini AR (2018) Collagen as coating material for 45S5 bioactive glass-based scaffolds for bone tissue engineering. *Int J Mol Sci* 19. <https://doi.org/10.3390/ijms19061807>
32. Deliormanli AM (2015) Preparation and in vitro characterization of electrospun 45S5 bioactive glass nanofibers. *Ceram Int* 41(1):417–425. <https://doi.org/10.1016/j.ceramint.2014.08.086>
33. Chen QZ, Thouas GA (2011) Fabrication and characterization of sol-gel derived 45S5 Bioglass®-ceramic scaffolds. *Acta Biomater* 7(10):3616–3626. <https://doi.org/10.1016/j.actbio.2011.06.005>
34. Zheng K et al. (2015) Aging time and temperature effects on the structure and bioactivity of gel-derived 45S5 glass-ceramics. *J Am Ceramic Soc* 98(1):30–38. <https://doi.org/10.1111/jace.13258>
35. Aalto-Setälä L, Uppstu P, Sinitsyna P, Lindfors NC, Hupa L (2021) Dissolution of amorphous s53p4 glass scaffolds in dynamic in vitro conditions. *Materials* 14. <https://doi.org/10.3390/ma14174834>
36. Zandi Karimi A, Rezaeibeigi E, Drew RAL (2018) Crystallization behavior of combeite in 45S5 Bioglass® via controlled heat treatment. *J Non Cryst Solids* 502(Dec):176–183. <https://doi.org/10.1016/j.jnoncrysol.2018.09.003>
37. Bellucci D, Anesi A, Salvatori R, Chiarini L, Cannillo V (2017) A comparative in vivo evaluation of bioactive glasses and bioactive glass-based composites for bone tissue repair. *Mater Sci Eng C* 79:286–295. <https://doi.org/10.1016/j.msec.2017.05.062>
38. Li H et al. (2020) Macro-/nanoporous Al-doped ZnO/cellulose composites based on tunable cellulose fiber sizes for enhancing photocatalytic properties. *Carbohydr Polym* 250(Dec):116873. <https://doi.org/10.1016/j.carbpol.2020.116873>
39. Lin CC, Huang LC, Shen P (2005) $\text{Na}_2\text{CaSi}_2\text{O}_6\text{-P}_2\text{O}_5$ based bioactive glasses. Part I: elasticity and structure. *J Non Cryst Solids* 351(40–42 Oct):3195–3203. <https://doi.org/10.1016/j.jnoncrysol.2005.08.020>
40. Baino F, Fiorilli S, Vitale-Brovarone C (2016) Bioactive glass-based materials with hierarchical porosity for medical applications: review of recent advances. *Acta Biomater* 42(Sep):18–32. <https://doi.org/10.1016/j.actbio.2016.06.033>. Elsevier Ltd
41. Dutta RC, Dey M, Dutta AK, Basu B (2017) Competent processing techniques for scaffolds in tissue engineering. *Biotechnol Adv* 35(2 Mar):240–250. <https://doi.org/10.1016/j.biotechadv.2017.01.001>. Elsevier Inc
42. Kukovecz Á, Kónya Z, Pálkó I, Mönter D, Reschtilowski W, Kiricsi I (2001) Surface fractal properties of morphologically different sol–gel derived silicates. *Chem Mater* 13(2):345–349. <https://doi.org/10.1021/cm001168m>
43. Kim JA, Lim J, Naren R, suk Yun H, Park EK (2016) Effect of the biodegradation rate controlled by pore structures in magnesium phosphate ceramic scaffolds on bone tissue regeneration in vivo. *Acta Biomater* 44:155–167. <https://doi.org/10.1016/j.actbio.2016.08.039>
44. Zamani D, Moztarzadeh F, Bizari D (2019) Alginate-bioactive glass containing Zn and Mg composite scaffolds for bone tissue engineering. *Int J Biol Macromol* 137(Sep):1256–1267. <https://doi.org/10.1016/j.ijbiomac.2019.06.182>
45. Srinivasan S, Jayasree R, Chennazhi KP, Nair SV, Jayakumar R (2012) Biocompatible alginate/nano bioactive glass ceramic composite scaffolds for periodontal tissue regeneration. *Carbohydr Polym* 87(1 Jan):274–283. <https://doi.org/10.1016/j.carbpol.2011.07.058>
46. Mecca FG, Bellucci D, Cannillo V (2023) Effect of thermal treatments and ion substitution on sintering and crystallization of bioactive glasses: a review. *Materials* 16. <https://doi.org/10.3390/ma16134651>
47. Lefebvre L et al. (2007) Structural transformations of bioactive glass 45S5 with thermal treatments. *Acta Mater* 55(10):3305–3313. <https://doi.org/10.1016/j.actamat.2007.01.029>
48. Huang LC, Lin CC, Shen P (2007) Crystallization and stoichiometry of crystals in $\text{Na}_2\text{CaSi}_2\text{O}_6\text{-P}_2\text{O}_5$ based bioactive glasses. *Mater Sci Eng A* 452–453(Apr):326–333. <https://doi.org/10.1016/j.msea.2006.10.136>
49. Shankhwar N, Srinivasan A (2016) Evaluation of sol–gel based magnetic 45S5 bioglass and bioglass–ceramics containing iron oxide. *Mater Sci Eng C* 62(May):190–196. <https://doi.org/10.1016/J.MSEC.2016.01.054>
50. Baino F, Fiume E (2019) Elastic mechanical properties of 45S5-based bioactive glass-ceramic scaffolds. *Materials* 12(Oct):19. <https://doi.org/10.3390/ma12193244>
51. Zeitler TR, Cormack AN (2006) Interaction of water with bioactive glass surfaces. *J Cryst Growth* 294(1 Aug):96–102. <https://doi.org/10.1016/j.jcrysgro.2006.05.029>
52. Par M et al. (2019) Long-term water sorption and solubility of experimental bioactive composites based on amorphous calcium phosphate and bioactive glass. *Dent Mater J* 38(4):555–564. <https://doi.org/10.4012/dmj.2018-145>
53. Khoshakhlagh P et al. (2017) Development and characterization of a bioglass/chitosan composite as an injectable bone substitute. *Carbohydr Polym* 157(Feb):1261–1271. <https://doi.org/10.1016/j.carbpol.2016.11.003>
54. Aki D, Ulag S, Unal S, Sengor M, Ekren N, Lin CC, Gunduz O (2020) 3D printing of PVA/hexagonal boron nitride/bacterial cellulose composite scaffolds for bone tissue engineering. *Mater Des* 196. <https://doi.org/10.1016/j.matdes.2020.109094>
55. Sepulveda P, Jones JR, Hench LL (2001) Characterization of Melt-Derived 45S5 and sol-gel-derived 58S Bioactive Glasses. <https://doi.org/10.1002/jbm.0000>
56. Kane RJ, Roeder RK (2012) Effects of hydroxyapatite reinforcement on the architecture and mechanical properties of freeze-dried collagen scaffolds. *J Mech Behav Biomed Mater* 7(Mar):41–49. <https://doi.org/10.1016/j.jmbbm.2011.09.010>
57. Yadav C, Maji PK (2019) Synergistic effect of cellulose nanofibres and bio-extracts for fabricating high strength sodium alginate based composite bio-sponges with antibacterial properties. *Carbohydr Polym* 203(Mar):396–408. <https://doi.org/10.1016/j.carbpol.2018.09.050>
58. Sarmast Sh M, George S, Dayang Radiah AB, Hoey D, Abdullah N, Kamarudin S (2022) Synthesis of bioactive glass using cellulose nano fibre template. *J Mech Behav Biomed Mater* 130(Jun):105174. <https://doi.org/10.1016/j.jmbbm.2022.105174>

59. Thavornutikarn B et al. (2017) Porous 45S5 Bioglass®-based scaffolds using stereolithography: effect of partial pre-sintering on structural and mechanical properties of scaffolds. *Mater Sci Eng C* 75(Jun):1281–1288. <https://doi.org/10.1016/j.msec.2017.03.001>
60. Feng B, Fang X, Wang HX, Dong W, Li YC (2016) The effect of crystallinity on compressive properties of Al-PTFE. *Polymers* 8(Oct):10. <https://doi.org/10.3390/polym8100356>
61. El-Rashidy AA, Roether JA, Harhaus L, Kneser U, Boccaccini AR (2017) Regenerating bone with bioactive glass scaffolds: a review of in vivo studies in bone defect models. *Acta Biomater* 62:1–28. <https://doi.org/10.1016/j.actbio.2017.08.030>
62. Si J, Cui Z, Wang Q, Liu Q, Liu C (2016) Biomimetic composite scaffolds based on mineralization of hydroxyapatite on electrospun poly(ϵ -caprolactone)/nanocellulose fibers. *Carbohydr Polym* 143:270–278. <https://doi.org/10.1016/j.carbpol.2016.02.015>
63. Chen J, Zeng L, Chen X, Liao T, Zheng J (2018) Preparation and characterization of bioactive glass tablets and evaluation of bioactivity and cytotoxicity in vitro. *Bioact Mater* 3(3):315–321. <https://doi.org/10.1016/j.bioactmat.2017.11.004>
64. Zheng K et al. (2015) Bio-templated bioactive glass particles with hierarchical macro–nano porous structure and drug delivery capability. *Colloids Surf B Biointerfaces* 135(Nov):825–832. <https://doi.org/10.1016/j.colsurfb.2015.03.038>
65. Luo H et al. (2016) Constructing a highly bioactive 3D nanofibrous bioglass scaffold via bacterial cellulose-templated sol-gel approach. *Mater Chem Phys* 176:1–5. <https://doi.org/10.1016/j.mtchemphys.2016.03.029>
66. Araújo M, Miola M, Baldi G, Perez J, Verné E (2016) Bioactive glasses with low Ca/P ratio and enhanced bioactivity. *Materials* 9:226. <https://doi.org/10.3390/ma9040226>
67. Moghanian A, Koohfar A, Hosseini S, Hosseini SH, Ghorbanoghli A, Sajjadnejad M, Sharifianjazi, F (2021) Synthesis, characterization and in vitro biological properties of simultaneous co-substituted Ti+4/Li+1 58s bioactive glass. *J Non-Cryst Solids*, 561. <https://doi.org/10.1016/j.jnoncrysol.2021.120740>
68. Zyman Z, Rokhmistrov D, Loza K (2013) Determination of the Ca/P ratio in calcium phosphates during the precipitation of hydroxyapatite using X-ray diffractometry. *Process Appl Ceramics* 7(2):93–95. <https://doi.org/10.2298/pac1302093z>
69. Ramlee SNL, Sharifulden NSAN, Mohamad H, Noor SNFM (2019) Sol-gel derived bioactive glass scaffolds incorporated with polyvinyl-alcohol and pluronic P123 polymers using sponge replication technique. *Mater Today Proc* 17:966–975. <https://doi.org/10.1016/j.matpr.2019.06.463>
70. Xiao J, Wei Q, Xue J, Yang Z, Deng Z, Zhao F (2022) Preparation and in vitro bioactivity study of a novel hollow mesoporous bioactive glass nanofiber Scaffold. *Molecules* 27. <https://doi.org/10.3390/molecules27227973>
71. Anand A et al. (2022) Influence of copper-strontium co-doping on bioactivity, cytotoxicity and antibacterial activity of mesoporous bioactive glass. *Gels* 8(11 Nov):743. <https://doi.org/10.3390/gels8110743>
72. Akhtach S, Tabia Z, Bricha M, El Mabrouk K (2021) Structural characterization, in vitro bioactivity, and antibacterial evaluation of low silver-doped bioactive glasses. *Ceram Int* 47(20 Oct):29036–29046. <https://doi.org/10.1016/j.ceramint.2021.07.066>
73. Luo L, Gong W, Yang X, Qin X, Liu W, Liu L, Ji L (2022) Preparation of super-long aligned mesoporous bioactive glass tubes by an aligned porous polystyrene template. *Mater Today Commun* 31. <https://doi.org/10.1016/j.mtcomm.2022.103309>
74. Li L, Hu H, Zhu Y, Zhu M, Liu Z (2019) 3D-printed ternary SiO₂ [sbn]CaO[sbn]P₂O₅ bioglass-ceramic scaffolds with tunable compositions and pores for bone regeneration. *Ceram Int* 45(8):10997–11005. <https://doi.org/10.1016/j.ceramint.2019.02.183>
75. Chen QZ, Ahmed I, Knowles JC, Nazhat SN, Boccaccini AR, Rezwani K (2008) Collagen release kinetics of surface functionalized 45S5 Bioglass®-based porous scaffolds. *J Biomed Mater Res A* 86(4):987–995. <https://doi.org/10.1002/jbm.a.31718>
76. Saravanapavan P, Jones JR, Pryce RS, Hench LL (2003) Bioactivity of gel – glass powders in the CaO-SiO₂ system: a comparison with ternary (CaO-P₂O₅ -SiO₂) and quaternary glasses (SiO₂ -CaO-P₂O₅ -Na₂O). *J Biomed Mater Res A* 66:17–19
77. Albert K, Huang XC, Hsu HY (2017) Bio-templated silica composites for next-generation biomedical applications. *Adv Colloid Interface Sci* 249(Nov):272–289. <https://doi.org/10.1016/j.cis.2017.04.011>
78. López-Ortiz S, Mendoza-Anaya D, Sánchez-Campos D, Fernandez-García ME, Salinas-Rodríguez E, Reyes-Valderrama MI, Rodríguez-Lugo V (2020) The pH effect on the growth of hexagonal and monoclinic hydroxyapatite synthesized by the hydrothermal method. *J Nanomater* 2020. <https://doi.org/10.1155/2020/5912592>
79. Ma G, Liu XY (2009) Hydroxyapatite: Hexagonal or monoclinic? *Cryst Growth Des* 9(7 Jul):2991–2994. <https://doi.org/10.1021/cg900156w>
80. Wang L, Nancollas GH (2008) “Calcium orthophosphates: Crystallization and Dissolution,”. *Chem Rev* 108(11 Nov):4628–4669. <https://doi.org/10.1021/cr0782574>
81. Liverina M, Schuhladden K, Orrú R, Cao G, Boccaccini AR, Liverani L (2020) Electrospun PCL/PGS composite fibers incorporating bioactive glass particles for soft tissue engineering applications. *Nanomaterials* 10. <https://doi.org/10.3390/nano10050978>
82. Dubey S, Mishra R, Roy P, Singh RP (2021) 3-D macro/microporous-nanofibrous bacterial cellulose scaffolds seeded with BMP-2 preconditioned mesenchymal stem cells exhibit remarkable potential for bone tissue engineering. *Int J Biol Macromol* 167(Jan):934–946. <https://doi.org/10.1016/j.ijbiomac.2020.11.049>
83. Begum S, Johnson WE, Worthington T, Martin RA (2016) The influence of pH and fluid dynamics on the antibacterial efficacy of 45S5 Bioglass. *Biomed Mater* 11(1 Feb):15006. <https://doi.org/10.1088/1748-6041/11/1/015006>
84. Mehrvarzfar P, Akhavan H, Rastgarian H, Akhlagi NM, Soleymannpour R, Ahmadi (2011) An in vitro comparative study on the antimicrobial effects of bioglass 45S5 vs. calcium hydroxide on enterococcus faecalis. *Iran Endodontic J* 6:29
85. Chen Q, Wu J, Liu Y, Li Y, Zhang C, Qi W,....., Pan, H (2019) Electrospun chitosan/PVA/bioglass Nanofibrous membrane with spatially designed structure for accelerating chronic wound healing. *Mater Sci Eng C*, 105. <https://doi.org/10.1016/j.msec.2019.110083>
86. Moghanian A, Nasiripour S, Hosseini SM, Hosseini SH, Rashvand A, Ghorbanoghli A,.....Jazi FS (2021) The effect of Ag substitution on physico-chemical and biological properties of sol-gel derived 60%SiO₂-31%CaO-4%P₂O₅-5%TiO₂ (mol%) quaternary bioactive glass. *J Non Cryst Solids* 560. <https://doi.org/10.1016/j.jnoncrysol.2021.120732>
87. Ciolek L et al. (2019) The studies of cytotoxicity and antibacterial activity of composites with ZnO-doped bioglass. *Int J Appl Ceram Technol* 16(2):541–551. <https://doi.org/10.1111/ijac.13144>
88. Doktorovova S, Souto EB, Silva AM (2014) Nanotoxicology applied to solid lipid nanoparticles and nanostructured lipid carriers – A systematic review of in vitro data. *Eur J Pharma Biopharma* 87(1 May):1–18. <https://doi.org/10.1016/J.EJPB.2014.02.005>

Publisher's note Springer Nature remains neutral with regard to jurisdictional claims in published maps and institutional affiliations.

Springer Nature or its licensor (e.g. a society or other partner) holds exclusive rights to this article under a publishing agreement with the author(s) or other rightsholder(s); author self-archiving of the accepted manuscript version of this article is solely governed by the terms of such publishing agreement and applicable law.